A Theoretical Investigation of Oxygen Carriers to Relieve Tissue Hypoxia in Cancer Therapy



Adam J. Bush
Keble College
University of Oxford

Submitted in partial fulfilment
of the requirements for the degree of

Master of Science by Research

Trinity Term 2021

Acknowledgments

Firstly, I must thank my supervisors, Professor Eleanor Stride and Professor Robin Cleveland, for their immeasurable support throughout this two-year research project. I am hugely grateful for their guidance, advice, and infinite patience on both technical and personal matters. I could not have asked for better supervisors.

Special thanks must also be given to Professor Costas Arvanitis and Yutong Guo at the Georgia Institute of Technology, where I was first inspired to delve into the world of oncology.

The BUBBL Laboratory at Oxford has been, and continues to be, an incredible research community to be a part of. This research would still be in its earliest phase were it not for the collaborations with Alexandra Vasilyeva and Emma Bluemke, and the daily discussions with Michael Newsome, Xinghao Cheng, and Karen Wendt. I look forward to working together during the next stage of the project.

On a personal note, none of this would have been possible without the unwavering support of my girlfriend, Katie.

This research project has been funded by the Medical Research Council (MRC) through the Oxford-MRC Doctoral Training Partnership (DTP).

Abstract

Oxygen-enhanced cancer therapy is a promising emergent strategy for treating aggressive malignancies such as pancreatic ductal adenocarcinoma. Reversal of the hypoxic tumour microenvironment (TME) through the application of biocompatible oxygen carriers may improve treatment outcomes using conventional therapies and/or enhance the efficacy of immunotherapies. There is currently limited understanding of the mechanisms by which these carriers, particularly oxygen micro and nanobubbles, deliver oxygen to hypoxic tumours. One hypothesis is that the oxygen carriers are reoxygenated on each pass of the circulation, when traversing the highly oxygenated alveolar capillaries, enabling ongoing deposition of oxygen. Another is that carriers enhance the rate of oxygen diffusion from red blood cells. Two computational models were developed to test these hypotheses *in silico*. The first model was used to simulate the molar oxygen flux from a monodisperse nanobubble population traversing the circulation. Reoxygenation of the injected nanobubbles was found to be a significant (> 90%) contributor to total oxygen deposition in the TME. Quantitatively, the predicted oxygen deposition was within the range of *in vivo* experimental data reported in Owen et al. (2016). To investigate the spatial and temporal variation in oxygen deposition within tumour tissue, a second model was developed which simulated the irregular tumour microvasculature in greater detail. Within this perfused TME model, varying oxygen diffusivity was observed to have minimal effect on the level of oxygen deposition, suggesting that reoxygenation of the nanobubbles is a more important mechanism for oxygen delivery.

Table of Contents

1	**Introduction**	**1**
1.1	Literature Review	1
1.1.1	Hypoxia in Pancreatic Cancer	1
1.1.1.1	Pancreatic Ductal Adenocarcinoma	1
1.1.1.2	Immunotherapy and Hypoxic Stress	2
1.1.1.3	Therapeutic Potential of Oxygen-Enhanced Immunotherapy	3
1.1.2	Therapeutic Oxygen Delivery	4
1.1.2.1	Methods of Therapeutic Oxygen Delivery	4
1.1.2.2	Mathematical Modelling of Oxygen Delivery	6
1.2	Research Objectives	9
1.2.1	Overview	9
1.2.2	The Oxygen Bubble Reoxygenation Hypothesis	10
1.2.3	The Bubble-Enhanced Oxygen Diffusivity Hypothesis	10
2	**Modelling the Recirculation of Injected Oxygen Nanobubbles**	**11**
2.0	Chapter Introduction	11
2.1	Part 1: Modelling the Dissolution of a Single Oxygen Bubble	13
2.1.1	Computational Domain and Physical Assumptions	13
2.1.2	Overview of Simulation Method	13
2.1.3	Validation of Code	16
2.1.4	Additional Modelling of CO_2	16
2.2	Part 2: Modelling Oxygen Circulation and Deposition in Tissue	17
2.2.1	Simulation Method: The Oxygen Bubble Recirculation Model	17
2.2.1.1	Overview	17
2.2.1.2	Governing Equations, Parameters, and Assumptions	18
2.2.1.3	Calculation of Oxygen Deposition in the Tumour Microenvironment	21
2.2.2	Simulation Conditions and Methods of Analysis	24
2.2.2.1	Comparison with *in vitro* Experiments	24
2.2.2.2	Replication of *in vivo* Conditions	24
2.2.2.3	Parametric Sensitivity Analysis	27
2.2.2.4	Investigating Intra-Arterial Injection	27
2.2.3	Results and Discussion	28
2.2.3.1	Comparison with *in vitro* Experiments	28
2.2.3.2	Replication of *in vivo* Conditions	30
2.2.3.2.1	Oxygen Bubble Molar Content and Radius	30
2.2.3.2.2	Oxygen Bubble Population	32
2.2.3.2.3	Tumour Oxygenation	33
2.2.3.3	Parametric Sensitivity Analysis	35
2.2.3.4	Investigating Intra-Arterial Injection	36
2.3	Part 3: Chapter Conclusions and Future Work	38

3	**Modelling the Distribution of Nanobubble-Released Oxygen in Tumour Tissue**	**40**
3.0	Chapter Introduction	40
3.0.1	Research Objectives	40
3.0.2	Overview of COMSOL Modelling Approach	41
3.1	Part 1: Oxygen Biodistribution in a Single-Capillary Tumour Microenvironment	42
3.1.1	Simulation Method	42
3.1.1.1	Oxygen Perfusion Model	42
3.1.1.2	Oxygen-Bubble Deposition Model	46
3.1.1.3	Fluid Mechanics Model	47
3.1.1.4	Single-Capillary Geometric Model	49
3.1.1.5	Single-Capillary Model Analyses	50
3.1.1.5.1	Validation of Model	50
3.1.1.5.2	Parametric Sensitivity Analysis	51
3.1.1.5.3	Investigating Bubble-Enhanced Oxygen Diffusivity	52
3.1.1.5.4	Sensitivity of Deposition to Tumour Metabolism	52
3.1.1.5.5	Sensitivity of Deposition to Capillary Inlet Oxygenation	52
3.1.2	Results and Discussion	53
3.1.2.1	Fluid Mechanics Model	53
3.1.2.2	Oxygen Perfusion Model	55
3.1.2.3	Oxygen-Bubble Deposition Model	57
3.1.2.4	Single-Capillary Model Analyses	62
3.1.2.4.1	Validation of Model	62
3.1.2.4.2	Parametric Sensitivity Analysis	63
3.1.2.4.3	Investigating Bubble-Enhanced Oxygen Diffusivity	66
3.1.2.4.4	Sensitivity of Deposition to Tumour Metabolism	67
3.1.2.4.5	Sensitivity of Deposition to Capillary Inlet Oxygenation	69
3.2	Part 2: Oxygen Biodistribution in a Heterogeneously Perfused Tumour Microenvironment	71
3.2.1	Simulation Method	71
3.2.1.1	Overview and Percolation-Based Vascular Geometry	71
3.2.1.2	Analysis of Nanobubble-Released O_2 Deposition	72
3.2.2	Results and Discussion	73
3.2.2.1	Fluid Mechanics and Steady-State Vascular Oxygen Distribution	73
3.2.2.2	Blood and Nanobubble-Released Oxygen Deposition in the Heterogeneously Perfused Tumour Microenvironment	76
3.3	Part 3: Chapter Conclusions and Future Work	81
4	**Overall Conclusions to Study**	**84**

5 References 86

6 Appendices 94
6.1 Appendix 1: Table of Transport Model Parameters 94

1 Introduction

1.1 Literature Review

1.1.1 Hypoxia in Pancreatic Cancer

1.1.1.1 Pancreatic Ductal Adenocarcinoma

Pancreatic cancer, specifically pancreatic ductal adenocarcinoma (PDAC), is associated with extremely poor prognoses. As of 2019 the global five-year survival rate is 9% (Rawla et al. (2019)), with a 6 - 9 month average survival following diagnosis (Siegel et al. (2018)). Surgical resection remains the only curative option, with a 15 - 20% five-year survival rate, but is restricted to early-stage tumours (approximately 15 - 20% of patients) (Ryan et al. (2014)). There is a multitude of factors contributing to poor clinical outcomes. Unresectable metastatic pancreatic cancers are common on account of the malignancy's aggressiveness, in addition to a lack of effective screening tests and the asymptomatic presentation of early-stage tumours (De La Cruz et al. (2014)).

Non-surgical treatment options for PDAC are limited on account of a hostile tumour physiology (Kleeff et al. 2016). Most significantly, pancreatic malignancies are characterised by a dense fibrous stroma (Ryan et al. (2014)) leading to a hypoxic tumour microenvironment (TME). Hypoxia is defined as the local deprivation of the oxygen supply to tissue, where the partial pressure of oxygen falls below 5 – 10 mmHg (Graham and Unger (2018)). There is not yet a universal definition for the hypoxic threshold partial pressure. Hypoxia in cancer arises as a result of abnormal angiogenesis giving rise to highly irregular vascularisation (Noman et al. (2019)). The resulting perfusion imbalance leads to regions in which local respiratory demand outweighs oxygen supply. In pancreatic tumours, median oxygen levels below 2.5 mm Hg have been recorded, contrasting with an average of 50 - 60 mm Hg in non-pathological pancreatic tissue (Koong et al. (2000)).

Hypoxic conditions are strongly correlated with poor patient outcomes (Wilson and Hay (2011), Maxwell et al. (1997)). Hypoxia-inducible transcription factors (HIFs) modulate the cellular response to hypoxic conditions (Zenewicz (2017), Krzywinska and Stockmann (2018)) and contribute to treatment resistance through various mechanisms. For example, hypoxia facilitates a more aggressive tumour phenotype in cancers with mutations in the p53 tumour suppressor gene (common in solid tumours such as PDAC) through resistance to HIF-1α-dependent p53-modulated apoptosis (Graeber et al. (1996)). Hypoxia-induced increased phenotypic survivability is thought to diminish the efficacy of all forms of oncological treatment (Shannon et al. (2003), Vaupel and Mayer (2007)).

1.1.1.2 Immunotherapy and Hypoxic Stress

Immunotherapy is a highly promising emergent strategy for treating multiple forms of cancer (Weinberg (2013), Byun et al. (2017)). In contrast to chemotherapy and radiation-based methods which halt tumour progression, immunotherapy enhances the host's immune system to induce a holistic cytotoxic response to cancerous cells (Whiteside et al. (2016)). As a result, immunotherapy affords the potential for patient specificity and continual immune surveillance (Jackson et al. (2011)). A variety of different therapeutic pathways can be used to augment a patient's tumour-immune response (for example using oncolytic viruses, CAR T-cells, or monoclonal antibodies), but all are primarily concerned with generating a cytotoxic T-cell lymphocyte (CTL) or natural killer cell (NK) response in the host (Chouaib et al. (2017)).

Hostile TME conditions suppress the physiological tumour-immune response and inhibit the capability of immunotherapies (Lee et al. (2010), Chang et al. (2016)). This is particularly problematic in pancreatic cancer. Clinical trials using various novel immunotherapeutic

approaches to treat pancreatic malignancies have exhibited zero to very limited clinical benefit (Kunk et al. (2016), Garrido-Laguna and Hidalgo (2015)).

Hypoxic stresses have been found to be immunosuppressive and immune-evasive, thereby reducing the curative potential of immunotherapy to treat advanced pancreatic cancers (Lequeux et al. (2019), Noman et al. (2019)). Hypoxia recruits immunosuppressive regulatory T-cells (Tregs), myeloid-derived suppressor cells (MDSCs) and tumour-assisted macrophage (TAM) cells which degrade the cytotoxic tumour immune response (Labiano et al. (2015)). Infiltration of CD8+ effector T-cells has also been found to be very low in hypoxic regions of pancreatic cancers (Noman et al. (2019)). Furthermore, HIF-1α upregulates programmed death ligand 1 (PD-L1) expression, reducing Treg apoptosis and CD8+ effector T-cell proliferation (Noman et al. (2014)). Metabolic alterations induced by the hypoxic environment repress CTL responses via tumour acidification, the generation of reactive nitrogen species and extracellular accumulation of adenosine (Chouaib et al. (2017)). Pro-phagocytic signals in macrophages and MDSCs are blocked by upregulated CD47 (Michaels et al. (2018)). HIFs upregulate vascular endothelial growth factor (VEGF) used to facilitate angiogenesis, aiding tumour motility, invasion and metastasis (Shweiki et al. (1995)) in addition to inhibiting tumour cell apoptosis (Pidgeon et al. (2001)).

1.1.1.3 Therapeutic Potential of Oxygen-Enhanced Immunotherapy

Reactivation of the tumour-immune response through alleviation of hypoxic stresses may therefore improve treatment outcomes (Wigerup et al. (2016)). Pre-clinical models have observed reactivated CTL and NK cell responses following respiratory hyperoxygenation (Hatfield et al. (2015)). Furthermore, Hatfield et al. found lower cytotoxic T lymphocyte-associated protein 4 (CTLA-4) levels in addition to reduced Treg infiltration. It has been

reported that oxygenation above 35 mmHg is required for passive immunotherapies (Hockel and Vaupel (2001), Chaplin et al. (1998)), with the sensitivity of immune checkpoint blockade (ICB) inhibitors to oxygen partial pressure currently unknown.

One of the hallmarks of an augmented tumour-immune response is the abscopal effect, whereby regression of secondary metastases is observed following treatment of the primary tumour (Ho et al. (2020)). Recent studies (currently under review) from Ulster University and the BUBBL laboratory at Oxford University have observed the abscopal effect in murine PDAC models following oxygen microbubble-enhanced sonodynamic therapy both with and without the addition of immunotherapy drugs. Sonodynamic therapy uses extracorporeal ultrasound to activate sonosensitive drugs in a targeted region specified by the ultrasonic focus (McEwan et al. (2015), Owen et al. (2016)). As cytotoxicity only occurs in the targeted region (the primary tumour mass), it is possible that the increased tumour oxygenation is augmenting the tumour-immune response, in line with conclusions in Hasan and Mazone (2015).

1.1.2 Therapeutic Oxygen Delivery

1.1.2.1 Methods of Therapeutic Oxygen Delivery

There are many clinically-approved oxygen delivery mechanisms available to patients. Hyperbaric oxygen (HBO) chambers isolate patients in an oxygen-rich (>21%) environment. These are typically used to treat carbon monoxide poisoning but have also been investigated for use in cancer therapy (Daruwalla and Christophi (2006)). A 2012 murine study found that HBO at 30% O_2 could induce tumour regression by reverting tumour cells to a p53 wild type thereby restoring the p53-mediated apoptosis mechanism (Gogna et al. (2012)). However, the majority of investigations have failed to indicate any clinical benefit for cancer patients

(Moen and Stuhr (2012)). The cost and operational requirements for using these chambers combined with the risk of oxygen toxicity renders them impractical for widespread cancer therapy (Khan et al. (2018)).

Haemoglobin-based oxygen carriers (HBOCs) are artificial blood substitutes which transport and deposit oxygen through the same mechanisms as red blood cells (Moradi et al. (2016)). The sigmoidal oxygen-haemoglobin dissociation curve facilitates high oxygen deposition in hypoxic regions (Adair (1926)). HBOCs therefore have significant clinical potential for use in blood transfusions. Clinical trials using HBOCs have been plagued by uncertain toxicity leading to poor patient outcomes (Alayash (2014)).

Biocompatible oxygen micro- and nanobubbles avoid many of these issues (Khan et al. (2018), Kheir et al. (2013)) and can be administered intravenously (IV) or orally (McEwan et al. (2015), Owen et al. (2016)). Microbubbles containing other gases (e.g. perfluorocarbons) have been in clinical use for several decades. They comprise a protein or phospholipid monolayer shell surrounding a gaseous core, with diameters typically ranging from 0.1 – 20 μm (Hernot and Klibanov (2008)). Microbubbles were initially developed as contrast agents for use in ultrasonic imaging due to their echogenicity (Gramiak and Shah (1968)) but have been investigated in a range of therapeutic applications (Ferrara et al. (2007)). For example, targeted delivery of encapsulated or surface-loaded therapeutics is made possible by application of extracorporeal ultrasound fields; low-intensity pulses can track microbubble positions in real time, with high-intensity ultrasound used to fragment the bubble and release the payload at a specified location (Stride (2009), Shpak et al. (2016)).

In addition to attaching drugs to the bubble surface, the core can be filled with bioactive gases, including oxygen, to promote therapeutic effects. McEwan et al. (2015) showed that oxygen microbubbles could be used to enhance the activity of a sonodynamic therapy drug in hypoxic tumours. Owen et al. (2016) showed that similar effects could be achieved with a suspension of oxygen nanobubbles (~200 nm in diameter). Delaney et al. (2019) observed a delay in tumour progression and improved survival in murine breast cancer brain metastases following radiation therapy supplemented by oxygen microbubbles. Fix et al. (2018) also reported improved tumour control when oxygen microbubbles were injected intratumourally immediately prior to radiotherapy.

1.1.2.2 Mathematical Modelling of Oxygen Delivery

In order to develop effective combination therapies using oxygen micro/nanobubbles it is important to first understand the extent to which tumour hypoxia can be alleviated. Simulations of physiological oxygen transport have primarily been focussed on modelling blood-oxygen content (comprising haemoglobin-bound and free plasma O_2) rather than oxygen contained within artificial carriers (Toma-Dasu and Dasu (2013), Popel (1989)).

Models of diffusive transport of free oxygen molecules are typically based on Fick's laws of diffusion (Fick (1855)). A well-known model of tissue oxygenation is the Krogh tissue cylinder; this model simulates radial diffusive transport between a single axial capillary and a cylindrical interstitium representing a region of perfused tissue, such as in solid tumours (Krogh (1919)). Common physical assumptions within Krogh tissue cylinders models include constant and uniform tissue oxygen consumption, diffusivity, and solubility. As these models focus on simulating the equilibrium tissue oxygen distribution arising from perfusion, all transport phenomena are modelled at the steady state. Additional physical complexity has

been incorporated through the introduction of intravascular transport resistance, pO_2-dependent oxygen consumption, myoglobin-mediated transport, and parallel capillary networks (Goldman (2008), Secomb (2015)). Diffusion-based models have also been developed to investigate oxygen transport in blood-perfluorocarbon mixtures within tubular vessels (Patel and Mehra (1997)).

The above models focus on simplified geometries for computational efficiency. Blood vessels in tumours, however, have been found to be highly irregular, with variation in diameter, tortuosity, and spatial distribution (Shannon et al. (2003), Secomb et al. (2004)); oxygen transport within the tumour microenvironment (TME) is strongly influenced by the heterogenous vascular architecture. For example, the blood-tumour barrier arises from regions of heightened vascular permeability to therapeutic molecules (Arvanitis et al. (2019)) and is also thought to influence oxygen transport (Toma-Dasu and Dasu (2013)). Multiple studies have therefore developed 2D and 3D computational models of the vascularised TME to study the penetration and distribution of both oxygen and cancer therapeutics (Dasu et al. (2003), Tsoukias et al. (2007), Arvanitis et al. (2018)).

Molecular oxygen transport from artificial carriers has been investigated *in silico* (Tao (1978), Kabalnov et al. (1998), Webb et al. (2010), Kwan et al. (2012)). Simulations of microbubbles are predominantly based on Fick's laws of diffusion, with various approaches used to characterise the permeability of the lipid boundary to gaseous species (Borden and Longo (2004), Sarkar et al. (2009)). Microbubbles are simulated singularly in the majority of studies, with the computational domain consisting of an infinite surrounding medium with constant physical properties (Sarkar et al. (2009), Kwan et al. (2012)). In reality, there will variability in the oxygen flux from therapeutic microbubbles in different regions of the

physiology. For example, heterogeneity in oxygen flux would result from the vascular oxygenation varying (by 0 - 100 mmHg) between and within different organs (Guyton and Hall (2016)).

Haemodynamic models of the circulatory system predominantly incorporate differential equations governing vascular properties within an electric circuit framework (De Pater and Van den Berg (1964), Liang and Liu (2005), Mossa (2008)). Unfortunately, it would be very difficult to amalgamate oxygen-bubble dissolution physics with these electrical-based cardiovascular network models in order to study oxygen release from an injected micro/nanobubble population. An alternative approach was therefore taken in the present study to investigate micro/nanobubble-released oxygen delivery to hypoxic tumours. This is described in the following sections.

1.2 Research Objectives

1.2.1 Overview

The goal of this research is to develop an understanding of the mechanisms by which oxygen micro/nanobubbles relieve tissue hypoxia. This could then lead to improvements in dosing strategies and delivery vehicle design to enhance oxygen delivery.

Significant increases in tumour oxygen levels, on the order of ~1000 Pa (~7.5 mmHg), have been observed in murine pancreatic cancer models following delivery of oxygen-loaded micro/nanobubbles (Owen et al. (2016), McEwan et al. (2015)). Interestingly, the oxygen partial pressures reported by Owen et al. were higher than could be explained by the quantity of oxygen contained within the bubbles. This may be due in part to an underestimation of the bubble concentration, but even with a revised concentration value (Vasilyeva (2019), there is still a considerable discrepancy as ~1000 Pa would represent over 0.5% of the initial oxygen capacity of the nanobubbles. With the proportion of the total murine blood flow passing though the tumour vasculature varying between 0.2 – 1% (NC3RS (2020)), when combined with the high rate of metabolic oxygen clearance within neoplastic tissue (Li et al. (2014), (Komar et al. (2009)) this suggests that the mechanism by which tumour oxygenation was occurring was not simply deposition of the initially encapsulated oxygen.

Two hypotheses have been proposed to explain this discrepancy: (i) oxygen bubbles remain in the circulation and act similarly to red blood cells, such that they are reoxygenated in the lungs and deliver additional oxygen to the tumour on each circulatory pass (Seekell et al. (2016); (ii) the carriers increase oxygen diffusivity within the plasma thereby increasing the rate of haemoglobin-released oxygen transport from blood cells to the vascular endothelium (Faithfull (1992)). Both of these hypotheses are investigated in this study.

1.2.2 The Oxygen Bubble Reoxygenation Hypothesis

The primary focus of the research within this thesis was an investigation of the influence of reoxygenation as a mechanism for enhancing the delivery of bubble-released oxygen to hypoxic tissue.

Chapter 2 documents the development of a novel computational approach to modelling the recirculation of injected oxygen bubbles within mammalian physiology, coupled to a simplistic model of oxygen deposition in tumour tissue.

Chapter 3 studies the delivery of oxygen to tumour tissue in greater detail for quantitative comparison with *in vivo* experimental data. A two-dimensional model of the hypoxic tumour microenvironment (TME) was developed to study the temporal and spatial heterogeneity in oxygen deposition. This model incorporates blood-oxygen delivery via perfusion, metabolic clearance of bubble- and blood-delivered oxygen, and a percolation-based geometry of the irregular tumour microvasculature.

1.2.3 The Bubble-Enhanced Oxygen Diffusivity Hypothesis

Relative to modelling bubble-oxygen recirculation, investigating bubble-enhanced oxygen diffusivity was a simpler task, only requiring adaptation of the TME model previously developed in Chapter 3. As such, these investigations are documented in the lattermost sections of Chapter 3 and comprise a smaller section of this thesis.

2 Modelling the Recirculation of Injected Oxygen Nanobubbles

2.0 Chapter Introduction

In this chapter, a computational model was developed to simulate the reoxygenation of injected oxygen nanobubbles within the circulatory system. This model consists of (i) a gas bubble dissolution model adapted from Kwan et al. (2012) which simulates gas transfer between oxygen bubbles and the surrounding medium coupled to (ii) an exponential-decay-based bubble population function within (iii) a novel computational framework representing the mammalian vasculature.

The bubble dissolution model was first verified against the results from the source paper (Kwan et al. (2012)) through comparison of simulation outputs using identical parameters and initial conditions. For use in physiological systems, this model was then adapted to incorporate the transport of carbon dioxide.

This work was followed by the development of the circulatory system model. This formed a computational framework within which the bubble-oxygen flux was simulated using the bubble dissolution model. Five distinct vascular environments (Veins, Lungs, Arteries, Normal Capillaries and Tumour Capillaries) were used to represent the mammalian circulatory system. A monodisperse bubble population was assumed; a single simulated bubble represented the injected population. Variations in bubble-oxygen content (via the dissolution model) were scaled by the total population size to determine the overall transfer of oxygen. An exponential decay function was incorporated to model the clearance of bubbles from the vasculature.

Oxygen release within the tumour vasculature was then used to calculate the resultant partial pressure within the tissue. As this chapter is focussed on investigating the influence of reoxygenation on the maximum quantity of oxygen that could be delivered, this oxygen deposition model was simplistic. Simulations assumed complete extravasation of bubble-released oxygen, a homogenous TME oxygen distribution, and zero metabolic clearance of oxygen by tumour cells.

2.1 Part 1: Modelling the Dissolution of a Single Oxygen Bubble

2.1.1 Computational Domain and Physical Assumptions

The oxygen dissolution model developed in Kwan et al. (2012) was used to simulate mass transfer between a clean or phospholipid-shelled oxygen microbubble (OxyMB) and an infinite surrounding medium. The bubble was assumed to be perfectly spherical, and therefore the system could be modelled as one-dimensional. Four gaseous species were modelled: oxygen, nitrogen, perfluorobutane (C_4F_{10}, also known as PFB) and water vapour. These species were assumed to behave as ideal gases. The phospholipid species modelled in the original publication were 1,2-dimyristoyl-sn-glycero-3-phosphocholine (DMPC), 1,2-dipalmitoyl-sn-glycero-3-phosphocholine (DPPC), 1,2-distearoyl-sn-glycero-3-phosphocholine (DSPC), and 1,2-dibehenoyl-sn-glycero-3-phosphocholine (DBPC).

2.1.2 Overview of Simulation Method

The number of moles of a gaseous species within the bubble was represented by n, and the equation for the molar flux of species i, $\frac{dn_i}{dt}$, was derived using Fick's Laws (Eq. 1).

$$\frac{dn_i}{dt} = -\frac{4\pi R^2 K_{H,i}}{\frac{R}{D_i}+\Omega_{s,i}}\left(\frac{2\sigma}{R} + P_H - \frac{3BT}{4\pi R^3}\sum_{j\neq i} n_j - f_i P_{sat,i}\right) \quad \text{Eq. 1}$$

R is the bubble radius; D is the diffusivity of each species in water; K_H is the species-specific Henry's constant (which converts dissolved concentrations into pressure terms); Ω_s is a resistance term that models the hindrance to species' permeation through the lipid shell; P_H is the hydrostatic pressure; $\frac{2\sigma}{R}$ is the Laplace pressure due to surface tension σ; P_{sat} is the partial pressure at saturation which, when multiplied by f, the saturation fraction, gives the partial pressure of species i dissolved in the surrounding medium; $\frac{3BT}{4\pi R^3}\sum_{j\neq i} n_j$ represented

the sum of the partial pressures of the other gaseous species (P_j) within the bubble (where B is the ideal gas constant and T is temperature).

An activation energy equation (Eq. 2) (Ciani et al. (2004)) was used to model the shell resistance Ω_s, which varies with the lipid-specific permeation resistance Ω_N in addition to the difference between the initial and time-varying bubble surface tension (σ_0 and σ respectively), the Boltzmann constant k_B, and the collision radius of each species a.

$$\Omega_{s,i} = \Omega_N e^{\frac{\pi a_i^2}{k_B T}(\sigma_0 - \sigma)} \quad \text{Eq. 2}$$

Collision radii were determined using an empirical relation between the critical temperature T_c and pressure P_c for each species (Eq. 3) (Tee et al. 1966). The empirical parameter ξ was measured as $0.118\ Pa^{\frac{1}{3}}K^{-\frac{1}{3}}m$.

$$\mathrm{a}_i = \frac{1}{2} * \xi \left(\frac{P_{c,i}}{T_{c,i}}\right)^{-\frac{1}{3}} * 10^{-9} \quad \text{Eq. 3}$$

The time-varying radius R of the bubble was found by consideration of the Laplace pressure due to surface tension, the hydrostatic pressure and the partial pressures of the species within the bubble (Eq. 4).

$$\frac{2\sigma}{R} + P_H - \frac{3BT}{4\pi R^3}\sum_i n_i = 0 \quad \text{Eq. 4}$$

Kwan and Borden (2012) developed a model of lipid shell mechanics using a time-varying surface tension term σ (Eq. 5-8). The linear elasticities of the lipid monolayer during expansion and compression (k_E and k_c respectively) determine the rate of change of σ. Further lipid-specific shell properties include the breaking tension σ_{break} (at breaking time t_{break}), equilibrium tension σ_{EQ}, and the tension recorded at maximum radius σ_{Rmax}. The initial radius R_0 and maximum radius reached R_{max} were used to calculate the areal strain for the lipid shell. Following rupture of the monolayer, a relaxation rate κ_E was used as a time constant during the expansion phase. Values for these parameters were all sourced from Kwan and Borden (2012).

If $R(t) < R_0$: $\sigma = 0$ Eq. 5

If $\sigma < \sigma_{break}$: $\sigma = k_E\left(\left(\frac{R(t)}{R_0}\right)^2 - 1\right)$ Eq. 6

If $R_{break} < R(t) < R_{max}$: $\sigma = \sigma_{EQ} + \left(\sigma_{break} - \sigma_{EQ}\right)e^{-\kappa_E(t-t_{break})}$ (Expansion) Eq. 7

If $R_{break} < R(t) < R_{max}$: $\sigma = \sigma_{Rmax} + k_c\left(\frac{R(t)^2 - R_{max}^2}{R_0^2}\right)$ (Compression) Eq. 8

The Newton-Raphson method was employed to computationally solve the non-linear differential equation (Eq. 1), with the time-step size set to ensure sufficient temporal resolution for modelling diffusion (Eq. 9). MATLAB R2019b (The Mathworks, Natick, USA) was used to perform the simulations.

$$\Delta t = \frac{R^2}{D_{max}} \quad \text{Eq. 9}$$

2.1.3 Validation of Code

Figure 1 shows simulation results using the code written for this study compared to data published by Kwan et al. (2012) under identical simulation conditions (Figures 1B and 6E in the original publication). This comparison validated the use of the code for further work in this study.

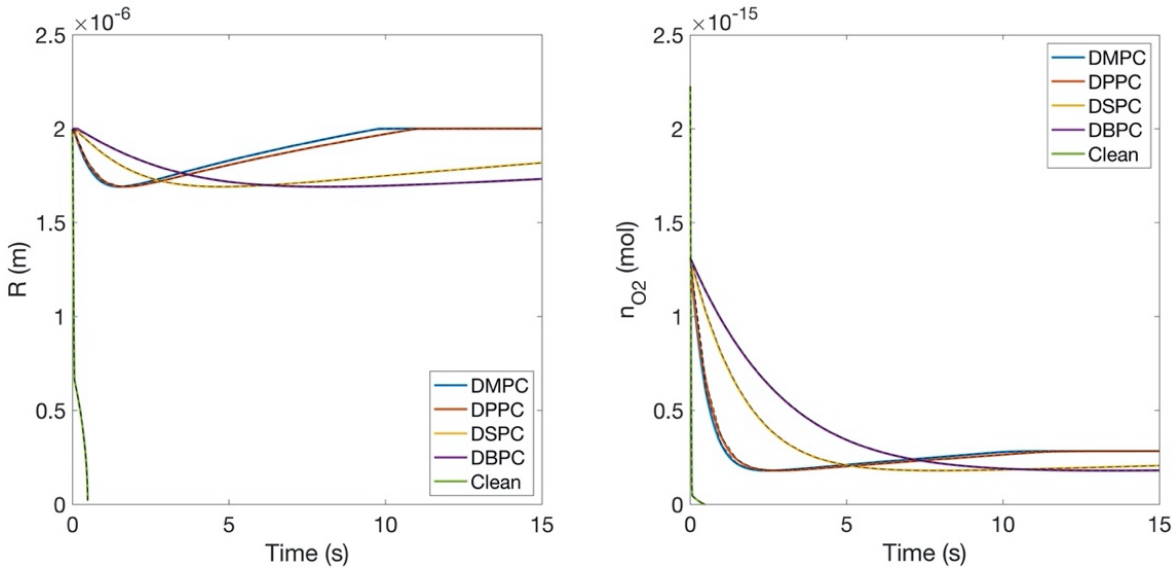


Figure 1: Time evolution of radius (left) and oxygen content (right) for a 2 µm-radius oxygen microbubble with varying lipid shell composition. Simulation results from the oxygen dissolution model developed in Kwan et al. (2012) (coloured lines) are compared with data from the source paper (dashed) for code validation.

2.1.4 Additional Modelling of CO_2

Due to the significant levels of carbon dioxide in the vasculature, CO_2 was included as an additional species in the oxygen dissolution model. The carbon dioxide parameters used were sourced from the same publications as for oxygen (Lide (2005), Sander (2015)) and the governing equations in the model were unchanged.

2.2 Part 2: Modelling Oxygen Circulation and Deposition in Tissue

2.2.1 Simulation Method: The Oxygen Bubble Recirculation Model

2.2.1.1 Overview

A numerical model was developed to investigate whether the reoxygenation of injected micro/nanobubbles contributes significantly to the total deposition of oxygen within hypoxic tumour tissue. Sensitivity studies were then used to determine which parameters were the most important factors for determining oxygen delivery.

Figure 2 shows a schematic of the oxygen bubble recirculation model. The circulatory system was modelled as five vascular environments, and in each environment the number of bubbles, N_{oxy}, and the bubble oxygen content, n_{O2}, was simulated. Simulations of the molar flux of oxygen and bubble clearance were used to predict oxygen delivery to the tumour.

Bubble transport through the circulation was simulated as follows. Initially, an IV bolus of micro- or nanobubbles is delivered to the systemic venous environment ("Veins" (V)) as it would be in practice. The bubbles then pass through the alveolar capillaries ("Lungs" (L) - this environment represented the entirety of the pulmonary vasculature), traverse the arterial network ("Arteries" (A)) and then enter the capillary network. The majority of bubbles travel through non-pathological "Normal Capillaries" (NC) and a small fraction of bubbles, ψ_T, traverse the hypoxic, abnormal tumour vasculature ("Tumour Capillaries" (TC)), whereupon the delivery of oxygen to the tumour microenvironment (TME) is determined. At the terminus of either type of capillary network, the bubbles re-enter the systemic venous system and the process is repeated.

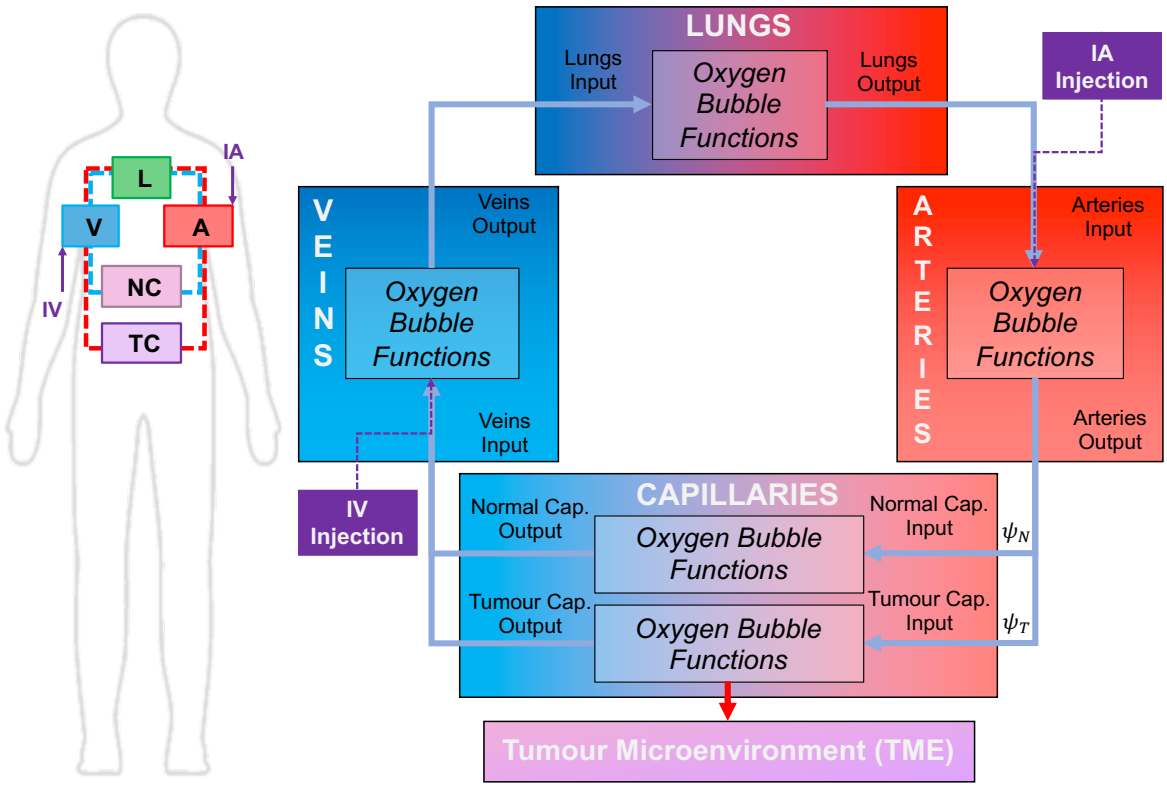


Figure 2: Schematic of the oxygen bubble recirculation model, consisting of five vascular environments (Veins (V), Lungs (L), Arteries (A), Normal Capillaries (NC), Tumour Capillaries (TC)) and the Tumour Microenvironment (TME). (Left) In-human representation, showing physiological pathway (blue) and pathological pathway (red). (Right) More detailed view, displaying input and output conditions associated with each environment. Oxygen deposition in the TME is represented by red arrow from the tumour capillaries. Capillary blood flow proportions, ψ, are shown. Intravenous (IV) and intra-arterial (IA) injection methods are shown.

2.2.1.2 Governing Equations, Parameters, and Assumptions

Each vascular environment was characterised by a set of parameters (Table 1), defining the properties of the fluid in which the bubbles were situated. Due to uncertainty in the detailed structure of oxygen nanobubbles (OxyNBs), for these simulations they were modelled in the same way as DBPC-coated oxygen microbubbles, but with a sub-micrometre radius and without a perfluorocarbon stabilizing agent in the core. Heterogeneity in the bubble population was not included in this model for simplicity. Therefore, single micro or nanobubbles, characterised by radius R, surface tension σ, and molar content n, were used to represent the average of a population. Incorporating a size distribution in future work will be important for capturing its influence on tumour oxygen deposition. Intravenous injection was

modelled (instead of oral delivery as in Owen et al. (2016)) as the efficiency of transport between the GI tract and bloodstream was unknown and because this was not relevant for testing the reoxygenation hypothesis in this study.

Env.	Blood Volume Fraction, f_v	Transit Time, τ	Half-life, $t_{\frac{1}{2}}$		P_{O2}	P_{N2}	P_{PFB}	P_{H2O}	P_{CO2}	P_H
			OxyNBs	OxyMBs						
	%	s			mmHg					
Veins	64 (A)	2.75	120 (A)	52 (A)	40 (E)	573 (E)	0	47 (E)	46 (E)	706
Lungs	16 (A)	0.69	120 (A)	52 (A)	104 (E)	569 (E)	0	47 (E)	46 (E)	760
Arteries	13 (A)	0.56	120 (A)	52 (A)	98 (E)	575 (E)	0	47 (E)	46 (E)	760
Normal Capillaries	7 (A) 6.5 w/out TC (A)	0.30	120 (A)	52 (A)	21 (E)	573 (E**)	0	47 (E**)	46 (E**)	687
Tumour Capillaries	0.5 ± 0.2 (B)	0.81 (C*)	250 (A)	72 (A)	2.5 (E)	573 (E**)	0	47 (E**)	46 (E**)	668.5

Table 1: Mouse circulatory system parameters used in the Oxygen Bubble Recirculation Model. Transit times were calculated via Equation 11. Half-lives were adapted from Wu et al. (2013). Total hydrostatic pressure, P_H, was calculated from the sum of individual species' partial pressures in the surrounding medium, P_i. *Capillary transit time was calculated using the ratio from normal to tumour tissue in humans from Aslan et al. (2019). ** N_2, H_2O, CO_2 partial pressures in normal and tumour capillaries were assumed equal to the systemic venous conditions. (A) Guyton and Hall (2016); (B) Komar et al. (2009); (C) Aslan et al. (2019); (D) Wu et al. (2013); (E) Beck (2008); (F) Koong et al. (2000)

The total quantity of oxygen encapsulated within the bubbles at a given point is the product of the oxygen content within an individual bubble, n_{O2}, and the number of bubbles, N_{oxy}. Bubble oxygen content n_{O2} was calculated using the oxygen dissolution model. If bubbles from the normal and tumour capillaries concurrently arrived at the veins, the radius R, surface tension σ and molar content n at the venous entrance ("Veins Input") was determined using a number-weighted average. Within the vessels, the plasma P_{O2} was assumed constant due to the quantities of oxygen released from the bubbles at a given position being of

negligible size relative to the total vascular oxygenation. In each vascular environment j, simulated for a transit time τ, clearance of the bubbles via the liver or destruction by other means was assumed to follow an exponential decay model with decay constant λ (Eq. 10).

$$N_{oxy_{output,j}} = N_{oxy_{input,j}} e^{-\lambda_j \tau_j} \quad \text{Eq. 10}$$

The environment-specific transit time, τ, was defined by the total blood transit time τ_{Total} multiplied by the blood volume proportion, f_v, (the proportion of the total blood volume located in each vascular environment j) (Eq. 11). The total transit time was determined by the total blood volume $V_{B\,Total}$ divided by the cardiac output C_O (Guyton and Hall (2016), Kreissl et al. (2006)) (Eq. 11).

$$\tau_j = f_{v,j} \cdot \tau_{Total} = f_{v,j} \cdot \frac{V_{B\,Total}}{C_O} \quad \text{Eq. 11}$$

The population decay constant, λ, was calculated from the half-lives of the bubbles, $t_{\frac{1}{2}}$, in each vascular environment j (Eq. 12).

$$\lambda_j = \frac{\ln(2)}{t_{\frac{1}{2},j}} \quad \text{Eq. 12}$$

In vivo data for bubble half-lives in the literature was limited. Wu et al. (2013) tabulated colorectal adenocarcinoma and normal organ $t_{\frac{1}{2}}$ values for Definity™ OxyMBs and 200 nm-diameter OxyNBs. However, with large variation in these data (see Table 1) in addition to a different OxyNB composition in this study, there was significant uncertainty in the $t_{\frac{1}{2}}$ values.

For simplicity, $t_{\frac{1}{2}}$ was assumed constant in non-pathological vessels (using the mean of normal organ $t_{\frac{1}{2}}$ values), changing only in the tumour vasculature.

Murine vascular transit times, τ, were calculated from Eq. 11 using C_O = 20 ml/min (Kreissl et al. (2006)) and $V_{B\,Total}$ = 1.46 ml (NC3RS (2020)). All other blood parameters in the mouse (f_v, P_i, $t_{\frac{1}{2}}$) were assumed unchanged from the human values.

2.2.1.3 Calculation of Oxygen Deposition in the Tumour Microenvironment:

Oxygen bubbles in the tumour capillaries were modelled as delivering oxygen to the tumour tissue via two processes. Bubbles destroyed in the tumour capillaries (number destroyed = $\Delta \mathrm{N}_{oxy_{TC}}$) released their entire oxygen payload (molar content = $n_{O2_{TC,input}}$) giving rise to $\Delta n_{O2,destr}$ (Eq. 13). Surviving bubbles (total number = $\mathrm{N}_{oxy_{TC,output}}$) released oxygen through dissolution (moles released per bubble = $\Delta n_{O2_{TC}}$) due to the oxygen concentration gradient between the bubble core and the surrounding fluid, giving rise to $\Delta n_{O2,rel}$ (Eq. 14).

$$\Delta n_{O2,destr} = \Delta \mathrm{N}_{oxy_{TC}} * n_{O2_{TC,input}} \quad \text{Eq. 13}$$

$$\Delta n_{O2,rel} = \mathrm{N}_{oxy_{TC,output}} * \Delta n_{O2_{TC}} \quad \text{Eq. 14}$$

The resulting total quantity of oxygen released into the TME, $\Delta n_{O2_{TME}}$, was the sum of the above processes multiplied by the fraction of oxygen molecules which diffuse into the TME, γ (Eq. 15).

$$\Delta n_{O2_{TME,i}} = \gamma \cdot \left(\Delta n_{O2,destr} + \Delta n_{O2,rel}\right) \quad \text{Eq. 15}$$

These simulations assumed $\gamma = 1$ and zero oxygen metabolism to give an upper bound for deposition in the tumour; oxygen was assumed to be retained within the TME for all simulated t. The resulting average oxygen concentration in the TME due to OxyMB/NB delivery, $\Delta c_{O2_{TME}}$, was given by $\Delta n_{O2_{TME}}$ divided by the TME volume V_{TME} (Eq. 16). The increased oxygen partial pressure in the TME, $\Delta P_{O2_{TME}}$, was this concentration divided by Henry's constant (Eq. 17).

$$\Delta c_{O2_{TME,i}} = \frac{\Delta n_{O2_{TME,i}}}{V_{TME}} \quad \text{Eq. 16}$$

$$\Delta P_{O2_{TME,i}} = \frac{\Delta n_{O2_{TME,i}}}{V_{TME} \cdot K_{H,O_2}} \quad \text{Eq. 17}$$

As these calculations were for a single circulatory pass, i, the total TME oxygen partial pressure was the sum of the individual oxygen deliveries over the simulated time period (Eq. 18).

$$\Delta P_{O2_{\substack{TME \\ Total}}} = \sum_i \Delta P_{O2_{TME,i}} \quad \text{Eq. 18}$$

A schematic of the computational code is shown in Figure 3, indicating the inputs, outputs, internal variables, and various functions used within the MATLAB script.

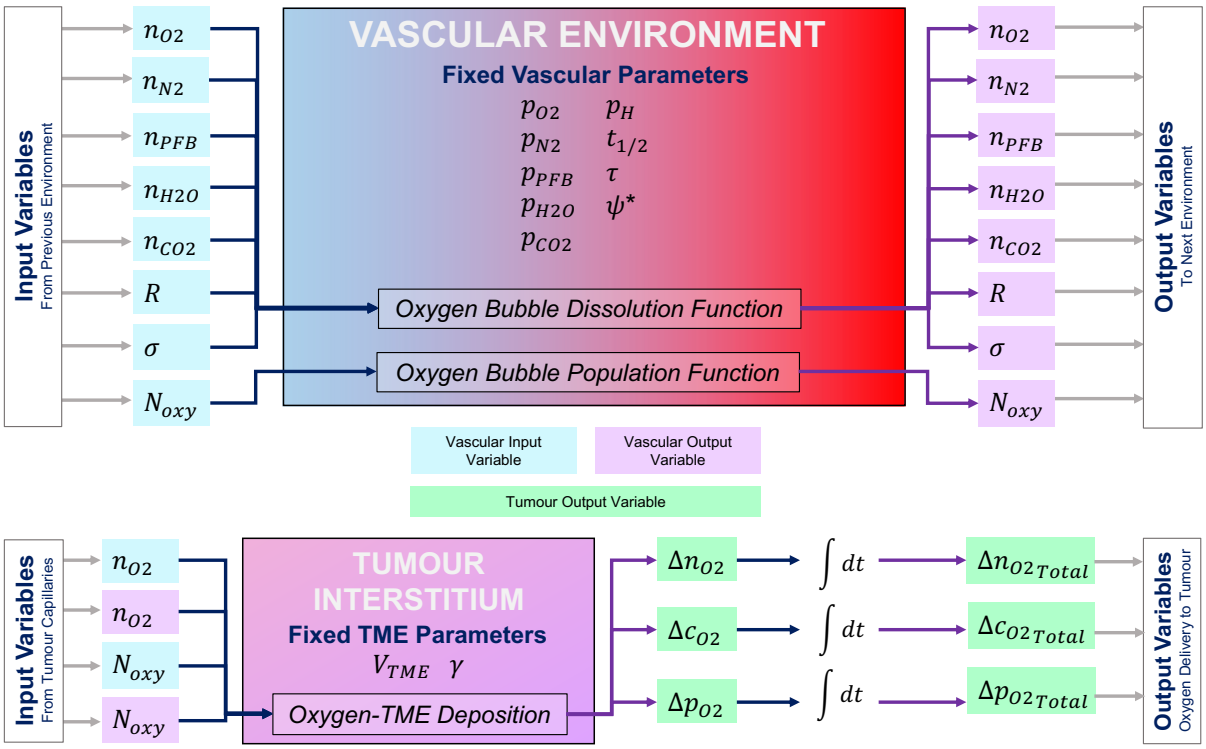


Figure 3: MATLAB script schematic for the oxygen bubble recirculation model. Vascular input (blue) and output (purple) variables, tumour output variables (green) and environment parameters are shown for a vascular environment *j* (top) and the tumour interstitium (bottom). *Variable for first circulation with IA injection. For non-capillary environments $\psi = 1$.

2.2.2 Simulation Conditions and Methods of Analysis

2.2.2.1 Comparison with *in vitro* Experiments:

The oxygen bubble recirculation model described above was first compared with *in vitro* experimental data from Owen et al. (2016) (using OxyNBs) and Thompson (2017) (using OxyMBs). These two studies measured the change in oxygen tension in a flow loop following a single OxyMB/NB injection.

A simplified single-environment ("Flow Loop") form of the oxygen bubble recirculation model simulated these conditions. Oxygen deposition in the suspension was calculated using Eq. 13-18, with the flow loop environment replacing the tumour capillaries, and the extravasation fraction, γ, set to 1. Flow loop partial pressures were set at atmospheric values.

2.2.2.2 Replication of *in vivo* Conditions

In order to investigate the contribution of bubble reoxygenation to the overall delivery of oxygen to tumour tissue, a study was conducted using simulation parameters derived from the *in vivo* and *in vitro* experimental conditions reported in Owen et al. (2016) and Vasilyeva (2019) respectively.

Owen et al. reported a tumour oxygenation of 600 ± 350 Pa. However, using the measured bubble concentration (3×10^7 bubbles/ml) the initial oxygen capacity of the nanobubbles was only 14.5 Pa. With identical preparation techniques, but more accurate bubble concentration and size distribution measurements, Vasilyeva (2019) reported 7×10^{12} bubbles/ml, a value 200,000 times higher. As shown in Table 2, using the same tumour volume the resulting maximum oxygen deposition using the Vasilyeva (2019) experimental conditions was over 10^4 times higher; with these values the reported oxygenation in Owen et al. (2016)

represented 0.4% of the initial oxygen capacity of the nanobubbles. As *in vivo* data were only reported in Owen et al. (2016), and the oxygen nanobubbles were prepared identically, the Vasilyeva (2019) parameters were used to compare the simulated tumour oxygenation relative to the experimental fibre-optic measurements.

Variable	Equation	Definition	Value	
			Owen et al. '16	Vasilyeva '19
R_0	-	OxyNB Radius (Monodisperse-equivalent)	430 nm	121.25 nm
$\bar{n}$	$\frac{P}{BT} \cdot \frac{4}{3}\pi R_0^3$	Average OxyNB Molar Content	1.36 x 10^{-17} mol/bubble	2.97 x 10^{-19} mol/bubble
$N_{oxy_{IV}}$	-	Initial Bubble Population	3 x 10^6 bubbles	1.4 x 10^{12} bubbles
V_{TME}	-	Tumour Volume	2.56 x 10^{-7} m^3	*
$\Delta n_{O2_{max}^{TME}}$	$N_{oxy_{IV}} \cdot \bar{n}$	Maximum Theoretical Oxygen Deposition in the TME	4.18 x 10^{-11} mol	4.16 x 10^{-7} mol
$\Delta c_{O2_{max}^{TME}}$	$\frac{\Delta n_{O2_{max}^{TME}}}{V_{TME}}$	Maximum Theoretical Oxygen Concentration in the TME from Nanobubble Delivery	1.59 x 10^{-4} mol/m^3	1.62 mol/m^3
$\Delta P_{O2_{max}^{TME}}$	$\frac{\Delta n_{O2_{max}^{TME}}}{V_{TME} \cdot K_{H_{O2}}}$	Maximum Theoretical Oxygen Partial Pressure in the TME from Nanobubble Delivery	14.5 Pa	1.48 x 10^5 Pa
$\Delta P_{O2_{obs}^{TME}}$	-	Oxygen Partial Pressure Observed in Murine Xenograft	600 ± 350 Pa	-

Table 2: *in vivo* experimental conditions in Owen et al. (2016) and Vasilyeva (2019). Maximum theoretical oxygen deposition in the mouse was calculated and contrasted with the observed increase in tumour oxygenation. * Vasilyeva (2019) did not study tumour oxygen levels; V_{TME} from Owen et al. (2016) was therefore used for comparison.

Additional simulation parameters for the oxygen bubble recirculation model are shown in Table 3. Simulations were computed for 125 circulations, rather than the ~420 circulations required to model 30 minutes of experimental time (as used in Owen et al. (2016)). This was done for computational simplicity, as the fractional increase in total oxygenation beyond this time was minimal. This is discussed further in the results section.

Variable	Definition	Value	Notes
t_{SIM}	Simulation Time	1800 s 540** s	Experimental Condition in Owen et al. (2016)
$n_{O2,0}$	Initial Condition for OxyNB Molar Content	2.97 x 10^{-19} mol	Calculated for OxyNB of Radius R_0
t_{CIRC}	Total Circulation Time	4.3 s	Guyton and Hall (2016), Kreissl et al. (2006)
γ	Extravasation Fraction	1.0	100% Extravasation Assumed in Model
ψ_T	Tumour Capillary Blood Flow Proportion	1%	*
ψ_N	Normal Capillary Blood Flow Proportion	99%	$1 - \psi_T$

Table 3: Simulation conditions replicating Owen et al. (2016). Note for simplicity this model simulated IV injection of the bubble suspension rather than oral delivery. *Murine ψ_T was determined through consideration of mean tumour volume (Owen et al. (2016)) and average mouse weight (NC3RS (2020)). **Simulation time was truncated to 125 circulations (540s) to reduce computational cost.

2.2.2.3 Parametric Sensitivity Analysis

As there was some uncertainty in the parameter values used within these models, the sensitivity of the predicted level of tumour oxygenation to variability in the parametric inputs was analysed. Variations in the total oxygen deposition in the TME were determined in response to ± 25% variation in $N_{oxy_{IV}}$, V_{TME}, ψ_T, τ_{TC}, $t_{1/2,j}$, $t_{1/2TC}$, $P_{O2_{TC}}$ and R_0. Parametric sensitivity simulations were computed for 50 circulations (215 s) for efficiency.

2.2.2.4 Investigating Intra-Arterial Injection

As there are different oxygen bubble administration methods used in laboratory experiments and in the clinic, it was decided to investigate the response of tumour oxygenation to intra-arterial (IA) injection as well as IV. To model intra-arterial injection, the initial condition for $n_{O2,0}$ and $N_{oxy_{IV}}$ was located at the input to the systemic arterial environment ("Arteries Input"). Additionally, ψ_T was varied from 1 - 100% for the first circulatory pass only. This factor was used to represent how close the arterial injection site was to the blood vessels which exclusively feed the tumour. Bubble transport through the circulation was otherwise unchanged from the IV simulations.

2.2.3 Results and Discussion

2.2.3.1 Comparison with *in vitro* Experiments

Simulated oxygen deposition in the flow loop using the *in vitro* conditions reported by Owen et al. (2016) and Thompson (2017), along with the experimentally reported data, is shown in Figure 4. In Figure 4 (left), using Owen et al.'s (2016) reported conditions, a significant disparity between experimental and simulation results was observed. The maximum measured P_{O2}, 52 kPa, was approximately 2000 times greater than the 0.03 kPa predicted in the simulations. This was, however, likely due to an error in the reported bubble concentration values as indicated in Section 2.2.2.2.

In Figure 4 (right), the much smaller discrepancies between the simulations and results reported by Thompson (2017) can be attributed to (i) uncertainty in the experimental parameter values and (ii) the assumption of a monodisperse bubble population. The decrease in the recorded *in vitro* P_{O2} after 400 s was most likely caused by unintentional oxygen leakage from the flow loop, as no reduction was recorded in the Owen et al. (2016) *in vitro* data. Simulated oxygen deposition occurred at a much faster rate than observed experimentally; 95% of maximal P_{O2} was reached within 4 s, compared with approximately 75 s *in vitro*.

One possible reason for this was that the simulations used a fixed vascular P_{O2}, resulting in a large concentration gradient drawing oxygen away from the bubbles. In the *in vitro* experiments, the oxygen concentration gradient would decrease in response to the increase in local P_{O2}, resulting in reduced oxygen transfer. Additionally, these simulations ignored any interactions between the individual bubbles, whereas concurrent deposition from OxyMBs in close proximity would reduce the oxygen concentration gradients thereby slowing efflux.

Further work could investigate the impact of modelling a heterogenous bubble population and a spatially varying vascular P_{O2} upon tumour oxygenation. It was deemed however that the results of the *in vitro* comparison work validated the model sufficiently for use in investigating the reoxygenation hypothesis.

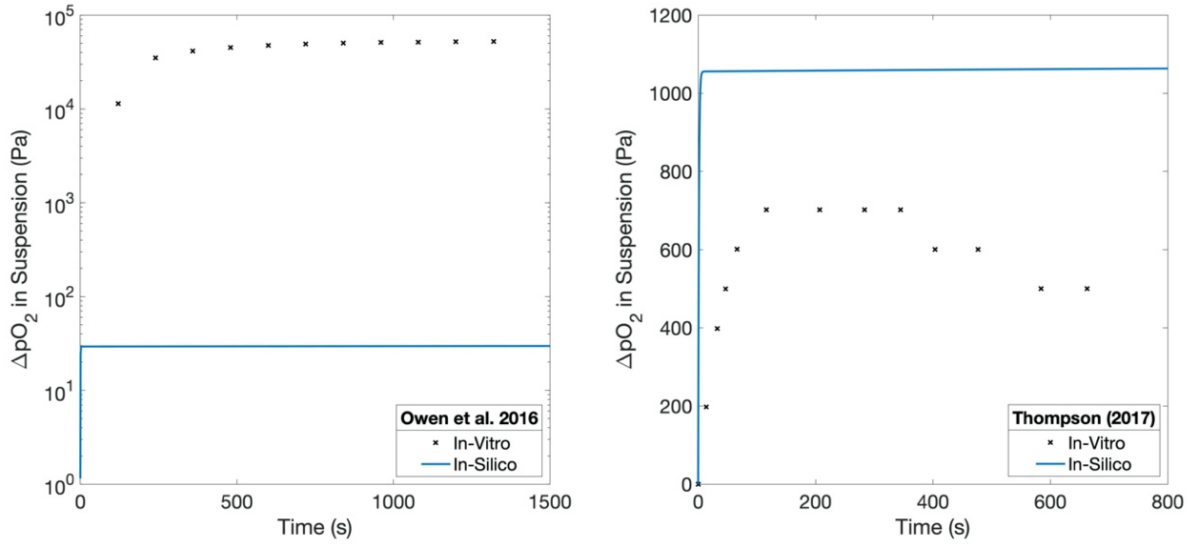


Figure 4: Flow loop simulation results using *in vitro* experimental conditions from (left) Owen et al. (2016) and (right) Thompson (2017). Oxygen deposition in the suspension was modelled over time using the oxygen dissolution model developed from Kwan et al. (2012).

2.2.3.2 Replication of *in vivo* Conditions

2.2.3.2.1 Oxygen Bubble Molar Content and Radius

In Figure 5, the simulated time variation in molar oxygen content for a single OxyNB is shown, using Vasilyeva (2019)'s experimental conditions. In both subfigures, the reoxygenation process is evident from the consistently higher output n_{O2} from the lungs and arteries compared to that from the venous and capillary environments.

Figure 5 (left) displays molar oxygen variation for the first 15 s. Within 2.7 s of the bubbles being injected, n_{O2} fell by 2.87 x 10^{-19} mol (96.5%) within the systemic venous environment. During the first complete circulation, n_{O2} fell by 97.5% for the physiological pathway (via the normal capillaries) and 99.5% for the pathological pathway (via the tumour capillaries). Oxygen efflux in the tumour capillaries, $\Delta n_{O2_{TC}}$, was approximately 1/13th as large as the venous efflux, Δn_{O2_V}, for the first circulation following injection. With the majority of initial oxygen release occurring far from the targeted region, this supported the investigation into intra-arterial injection.

Arterial output n_{O2} was lower than that from the lungs, which is coincident with higher p_{O2} in the latter. As the difference in p_{O2} between these vascular environments was minimal (Table 2), this suggests that mass transfer between the OxyNB and surroundings had reached an equilibrium state within the alveolar capillaries, similarly to red blood cells (Guyton and Hall (2016)). Red blood cells rely on reoxygenation within the circulatory system to continually supply tissues with oxygen, and therefore these results suggest that the nanobubbles could behave similarly.

The variation in n_{O2} over the total simulation time (125 circulations) is shown in Figure 5 (right). The extent of reoxygenation diminished sharply, with n_{O2} measured at the outputs of the lungs and tumour capillaries falling by 95% and 96% respectively within 200 s. This can be attributed to two separate mechanisms: (i) replacement of the gaseous oxygen with nitrogen from the surroundings and (ii) overall dissolution of the OxyNB over time.

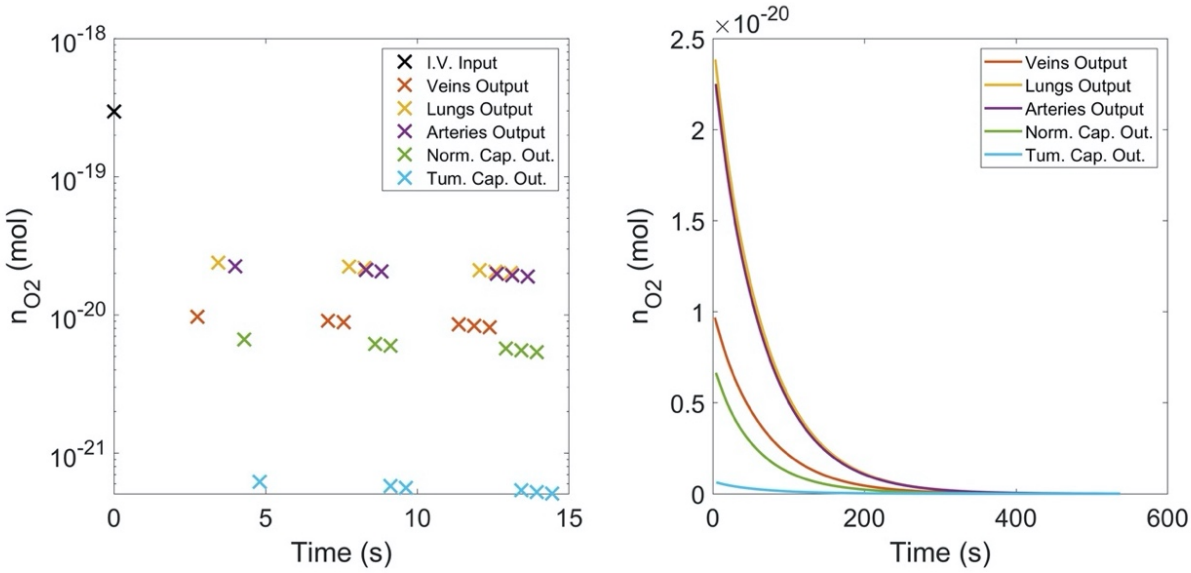


Figure 5. Time variation in OxyNB oxygen molar content at the output of each vascular environment. New circulatory loops were initiated at the terminus of capillary environments. (Left) Discrete data were plotted for 4 circulations to highlight the process of reoxygenation. (Right) Data plotted continuously for 125 circulations to highlight the dissolution of the OxyNB over time.

Molar flux within the OxyNB during the first circulatory pass is shown in Figure 6 (left). Nitrogen influx is immediately apparent; n_{N2} exceeded n_{O2} before 25% of the first venous transit had elapsed, and nitrogen remained the dominant species thereafter. This was expected given the relative partial pressures of the two species (Table 1).

Figure 6 (right) displays the nanobubble radius decreasing over time due to dissolution of the encapsulated gas into the surrounding fluid medium. In the literature, nanobubble size has been reported to remain stable for periods on the order of hours (Khan et al. (2018)).

However, at t = 500 s within this model the OxyNB radius had fallen by 95% to 6 nm, from over 120 nm initially. As the OxyNBs were simulated using a model based on OxyMB physics, this dissolution process may have been overestimated. Developments made in modelling nanobubble-specific dissolution physics should therefore be incorporated within this model in the future.

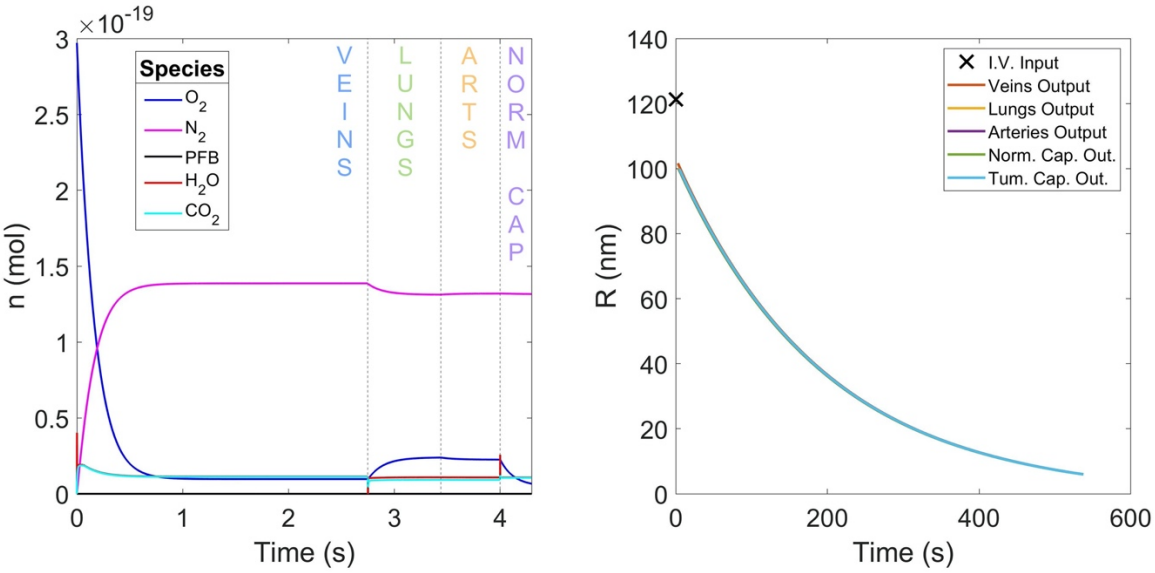


Figure 6: (Left) Variation in molar content for all gaseous species for the first circulation. Vascular environments are clearly delineated. (Right) Time variation in bubble radius, measured in nanometres, showing the dissolution of the OxyNB over time.

2.2.3.2.2 Oxygen Bubble Population

Figure 7 (left) displays the variation in the oxygen bubble population over time. The primary bubble population was defined as bubbles which had not passed through the TME vasculature, with secondary populations containing bubbles which had passed through the tumour capillaries at least once. As shown, the primary OxyNB population N_{oxy_P}, measured at the tumour capillaries' input, underwent exponential decay. With ψ_T = 0.01, the first-pass $N_{oxy_{P,}}$ was 1% of $N_{oxy_{IV}}$. After 300s, $N_{oxy_{P,}}$ had fallen to 0.1% of $N_{oxy_{IV}}$ and by 500s it had decreased to 0.02% of $N_{oxy_{IV}}$ as expected.

With a single bifurcation in the capillary network (Figure 2), at certain t there was concurrent arrival of different secondary-population OxyNBs at the systemic venous input. Therefore, ${N_{oxy}}_{TC,input}$ for these populations did not follow a simple exponential tail. However, bubble populations emerging from the tumour capillaries were much smaller than the primary population, and thus had a relatively minimal effect on the overall oxygen deposition curve.

2.2.3.2.3 Tumour Oxygenation

Total oxygen deposition in the TME is shown in Figure 7 (right). Relative to the research objectives for this section, the deposition data support the reoxygenation hypothesis. Following injection, the oxygen deposition from the first circulation, 106 Pa, accounted for 8.5% of the total tumour oxygenation measured. From this point, any addition oxygen delivered to the tumour tissue (91.5% of the total) was due to nanobubbles which had been reoxygenated in the lungs.

As noted in Section 2.2.3.2.1, the stability of the oxygen nanobubbles, and thus their effective lifetime in the circulatory system, was likely underestimated by the bubble dissolution model. With a reduced circulation lifetime, the extent to which the nanobubbles are reoxygenated and then deposit oxygen in the tumour would also be reduced. Therefore, the simulations of tumour oxygenation represent an underestimate of the importance of the reoxygenation mechanism, as it is likely that more than 91.5% of the total oxygen delivered to tumour tissue would occur via reoxygenated nanobubbles.

With zero clearance in the TME, $\Delta {P_{O2}}_{\substack{TME \\ Total}}$ rose to a maximum of 1240 Pa at t = 540 s, which was equivalent to 0.85% of the initial oxygen capacity of the injected nanobubbles (148 kPa) (Table 2). This maximum value was of a similar order to magnitude to the *in vivo*

measurement (600 ± 350 Pa) in Owen et al. (2016). It is important to note, however, that the *in vivo* measurements were only taken at a single point within the murine tumour xenograft and that the simulations assumed a homogenous oxygen distribution within the TME and omitted the metabolic clearance of oxygen. Chapter 3 investigates spatially and temporally heterogenous oxygen deposition within a vascularised TME model, for qualitative comparison with the experimental data.

The data in Figure 7 (right) justified the truncation of the simulation time, as minimal tumour oxygenation would be expected beyond t = 540 s. When simulating only 50 circulations, which required only 0.9% of the computational time compared with 125 circulations, the tumour oxygenation reached 98.8% of its maximum value. This was considered acceptable for use in the following parametric sensitivity and intra-arterial studies.

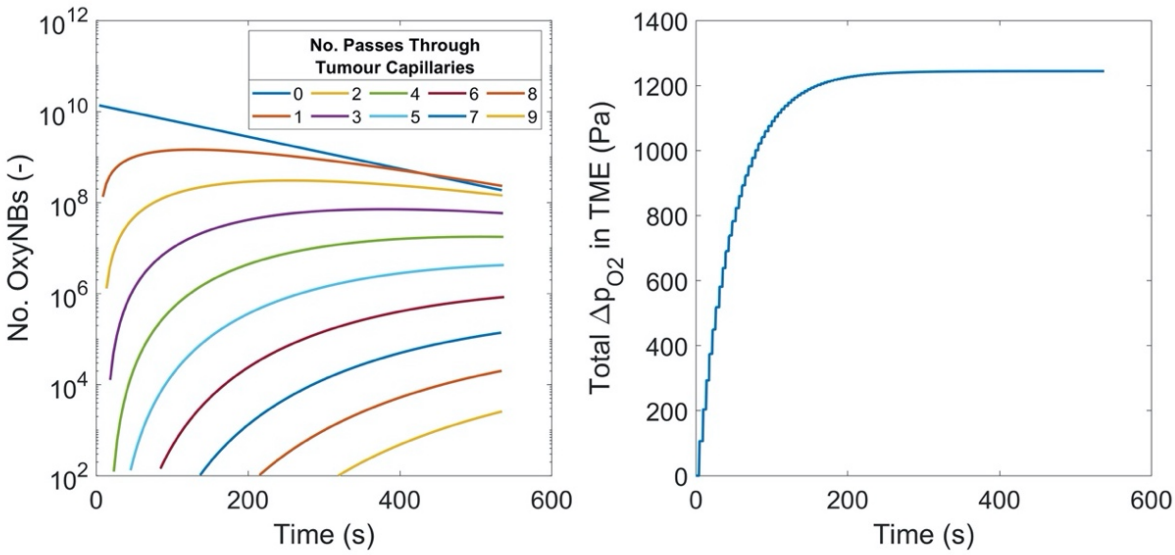


Figure 7: (Left) Time variation in OxyNB population size, measured at the input to the Tumour Capillaries. Secondary bubble populations arise due to the bifurcation between capillary environments. Ten populations are shown. (Right) Oxygen deposition in the TME using Vasilyeva (2019) *in vitro* experimental conditions, simulated to 125 circulations.

2.2.3.3 Parametric Sensitivity Analysis

The sensitivity of total oxygen deposition to each of the simulation variables is displayed in Figure 8. As expected, there was a directly proportional response to changes in both N_{oxy} and ψ_T and an inversely proportional response to changes in V_{TME}. The sensitivity to variations in $P_{O2_{TC}}$ and $t_{\frac{1}{2}TC}$ was very limited (< 1%). Sensitivity to τ_{TC} and $t_{\frac{1}{2}(all),}$ was positive and non-linear with 4% and 3% greater responses to negative variation respectively.

High sensitivity to bubble radius was observed; the total oxygen deposition in the tumour increased by 75% in response to a 25% greater R_0 value. This result was expected, as the oxygen content within a nanobubble is proportional to the cube of the radius. As noted previously, this study assumed a monodisperse nanobubble population for computational simplicity. In reality, the bubbles will have a size distribution; the nanobubble radii reported in Vasilyeva (2019) ranged from 15 - 250 nm. Investigating the feasibility of incorporating size distributions within the dissolution model is therefore a pertinent area for future work.

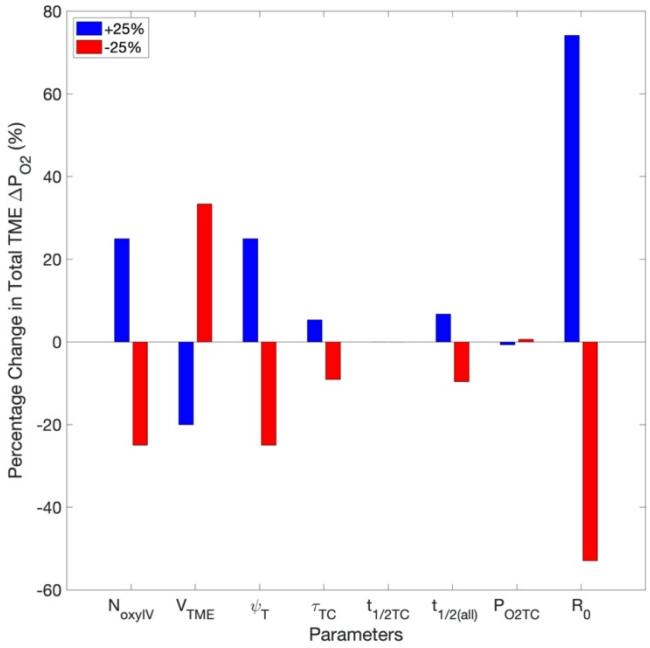


Figure 8: Parametric sensitivity analysis, measuring the percentage change in maximum cumulative P_{O2} value in response to ±25% variation in several key simulation parameters.

2.2.3.4 Investigating Intra-Arterial Injection:

Analysis of the tumour oxygenation data exposed a potential physiological sensitivity that could be significant for the clinical application of oxygen-bubbles in cancer therapy. The highest oxygen deposition occurred during the first circulatory pass and comprised 8.5% of the total tumour oxygenation. Due to the very high oxygen efflux (96.5%) from the nanobubbles during the first venous transit, relocating the injection site closer to the tumour entrance was hypothesized to generate a much larger oxygen deposition in the tumour.

As observed in Figure 9 (left), using IA injection there was a linear relationship between tumour oxygenation and ψ_T (first circulation only), with a gradient of 146 Pa / percentage ψ_T. Using IA delivery, the proportion of oxygen delivery to the TME relative to the initial capacity of the injected nanobubbles ranged from 0.9% - 10.6% (with a corresponding first pass ψ_T of 1 - 100%). Relative to IV delivery, the predicted average oxygenation was 10 times greater using IA injection with 75% first-circulation ψ_T. Relocating the injection site such that the OxyMB/NBs are in closer proximity to the splenic or superior mesenteric arteries would therefore be predicted to contribute to significantly greater total oxygen delivery to pancreatic tumours.

With better injection position, the first-pass oxygen deposition also contributed to an increasingly greater proportion of the total tumour oxygenation (Figure 9, right), signifying that the pharmacokinetic profile of oxygen delivery may also be sensitive to the injection site's location. Whilst *in vivo* tumour oxygenation is also dependent on the rate of metabolic clearance, these results suggest it may be possible to tailor the dosing regime and delivery method fit a desired pharmacokinetic profile (for instance, to maximise the efficacy of a co-injected immunotherapeutic).

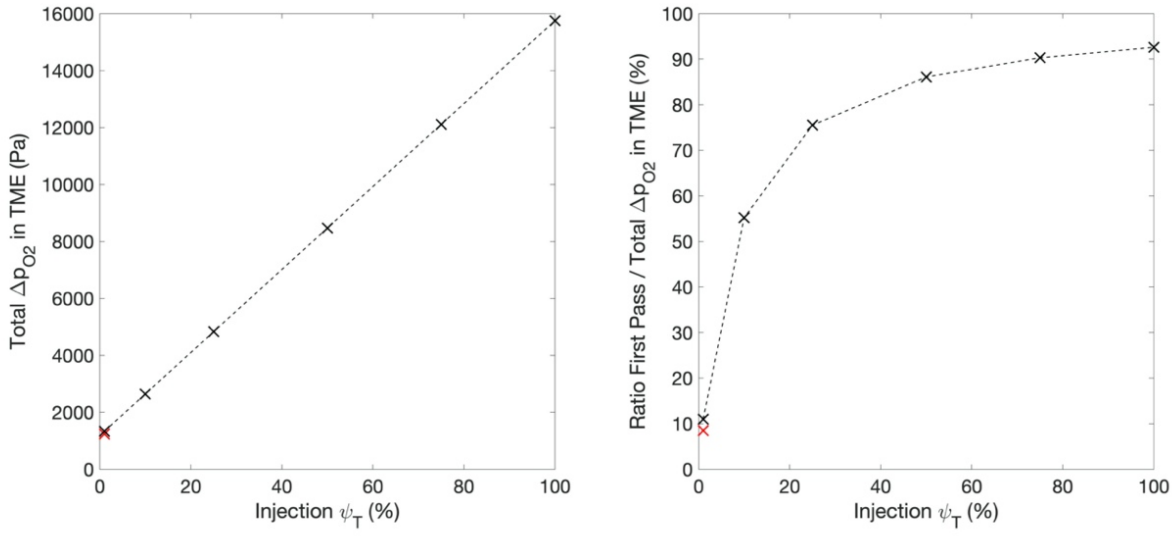


Figure 9. Investigating intra-arterial (IA) injection for OxyMB/NBs. (Left) Response of the total tumour oxygenation to first-circulation-variable ψ_T. (Right) Variability in the ratio of first-pass to total TME oxygenation with first-circulation-variable ψ_T. IV data points are plotted in red for comparison.

These conclusions may have direct clinical relevance. Intra-arterial delivery has higher clinical complexity and risk but finding an approachable arterial delivery site could increase the tumour oxygenation tenfold or greater compared to IV. Raising the tumour ΔP_{O2} above the immuno-suppressive hypoxic threshold (Hockel and Vaupel (2001)) may therefore be significantly easier using this delivery method. Furthermore, if the majority of tumour oxygenation occurred immediately following IA delivery as predicted, the oxygen dosing could be tailored for each patient to fit the optimal pharmacokinetic/dynamic profile for the therapeutic.

2.3 Part 3: Chapter Conclusions and Future Work

In simulations recreating the *in vivo* experimental conditions in Owen et al. (2016), using the updated nanobubble properties from Vasilyeva (2019), the reoxygenation of injected oxygen nanobubbles was found to be a significant contributor to tumour oxygenation; over 90% of the total oxygen deposition within tumour tissue was predicted to arise from reoxygenated nanobubbles. Additionally, the volume-averaged oxygen deposition predicted within the TME (1240 Pa at the maximum point) was of a similar order to the experimentally observed oxygen deposition (600 ± 350 Pa) in Owen et al. (2016). The total oxygen deposition in the tumour was found be highly sensitive to bubble size and concentration and to tumour volume and vascularity, as would be expected. The simulations also indicated that higher levels of oxygen deposition could be achieved with the initial injection by changing the administration regime from intravenous (IV) to intra-arterial (IA).

Whilst these results support the reoxygenation hypothesis, the oxygen bubble recirculation model assumed (i) a homogenous distribution of nanobubble-delivered oxygen and (ii) zero metabolic clearance within the tumour tissue. The next step for this study was therefore to develop a perfused TME model. This work is documented in Chapter 3.

Regarding other areas for future work not pursued in this thesis, the primary area of focus should be to incorporate nanobubble-specific dissolution physics within the recirculation model. At the time of writing, there is unfortunately insufficient characterisation data available on which to build a nanobubble-specific model, and the simulations of dissolution consequently predicted an underestimation of stability relative to experimental observations. As the extent of reoxygenation is dependent on the size and stability of the nanobubbles, it is hoped that improved dissolution models can be developed in the future.

In addition, the disparities between the predicted and experimental oxygen deposition profiles were thought to be partially due to the singular nature of the bubble dissolution model. The feasibility of modelling the interactions between multiple nanobubbles in suspension should therefore also be investigated.

Furthermore, the total oxygen deposition was observed to be highly sensitive to the initial nanobubble radius. For computational simplicity, and due to a lack of radius-dependent half-life data in the literature, a monodisperse nanobubble population was assumed in this study. Future work should therefore endeavour to incorporate heterogeneity in the size distribution (and corresponding half-life) of the nanobubbles, in order to more accurately represent the characteristics of the injected population.

3 Modelling the Distribution of Nanobubble-Released Oxygen in Tumour Tissue

3.0 Chapter Introduction

3.0.1 Research Objectives

Following from the Oxygen Bubble Recirculation Model developed in Chapter 2, this chapter documents the study of bubble-released oxygen deposition in a vascularised tumour microenvironment (TME) model. Whilst the reoxygenation of injected oxygen nanobubbles was shown to be a viable hypothesis, a more sophisticated model is required to make a valid comparison with the *in vivo* results reported in Owen et al. (2016).

In Chapter 2, the modelling of the deposition of the nanobubble-released oxygen within the TME assumed zero metabolic clearance and that the released oxygen was homogenously distributed throughout the tissue. Furthermore, blood-oxygen perfusion was not modelled. In order to generate accurate predictions of oxygen deposition within the heterogenous tumour physiology, additional mechanisms were required within the TME model.

The computational model developed in this chapter simulates a two-dimensional perfused tumour microenvironment, which incorporates diffusive and convective oxygen transport together with metabolic clearance and geometric heterogeneity. Additionally, the pre-existing steady-state tissue oxygenation due to blood perfusion was calculated to accurately model the deposition of nanobubble-released oxygen. This was required due to the non-linear dependence of diffusive transport and metabolic clearance on the spatial distribution of oxygen within the tissue and vasculature (Goldman (2008)). The new TME model was also used to investigate bubble-enhanced diffusivity as a mechanism for increased tumour oxygenation relative to the injected oxygen capacity. The importance of this mechanism relative to the reoxygenation of the injected nanobubbles was then evaluated.

3.0.2 Overview of COMSOL Modelling Approach

In this study, a two-dimensional computational model was developed in COMSOL Multiphysics 5.5 (COMSOL Incorporated, Stockholm, Sweden) to simulate the deposition of oxygen by blood cells and circulating nanobubbles in the microenvironment of (i) a single linear capillary and (ii) a vascular network. A complete list of parameters used in this model can be found in Appendix 1.

The study involved two computational steps. The first step, the stationary solver, computed the steady-state perfusion of tissue. This modelled oxygen deposition from the blood cells to the interstitium and the associated fluid velocity and hydrostatic pressure fields. The second step, the time-dependent solver, modelled the time-varying release of oxygen from the injected nanobubbles. This was initialised using the steady-state results computed previously.

The oxygen transport model used in this study was based on Lucker et al. (2014) but adapted for computational simplicity. In contrast to the source paper, a single continuous vascular domain containing both free and bound oxygen was assumed, rather than modelling discrete erythrocytes within a separate plasma compartment.

An initial study was conducted using a single capillary geometry to (i) evaluate the predicted vascular oxygen distribution relative to experimental data and (ii) explore the spatial and temporal variation of oxygen deposition in the surrounding tissue. This was followed by a more complex percolation-based vascular network model, which was used to investigate the heterogeneity in the distribution of nanobubble-released oxygen. These results were then compared with the *in vivo* experimental data reported in Owen et al. (2016).

3.1 Part 1: Oxygen Biodistribution in a Single-Capillary Tumour Microenvironment

3.1.1 Simulation Method

3.1.1.1 Oxygen Perfusion Model

The oxygen transport model developed in Lucker et al. (2014) was adapted for use in this study. Lucker et al. developed a three-domain transport model, in which individual red blood cells (subscript: *RBC*) suspended in the blood plasma (subscript: *PL*) deliver oxygen to a surrounding interstitium (subscript: *int*). In contrast, the adapted model developed for this study used a continuum approach with two computational domains, the blood (subscript: *RBC*) and the interstitium (subscript: *int*). The reasoning for this was twofold. Firstly, plasma oxygen is frequently disregarded in computational models (Goldman (2008)) as it can be assumed to be unchanged relative to the intra-RBC free oxygen concentration and represents only a very small fraction of the total blood-O_2 content. Secondly, the percolation-based geometry used to later model the irregular tumour vasculature (Arvanitis et al. (2018)) consisted of only two domains. Incorporating an additional plasma region into this latter model would have required significantly greater computational complexity.

Within the transport model, two distinct states of oxygen were modelled: free and haemoglobin-bound. Free oxygen was present in all of the computational domains, and was represented by its concentration c, and corresponding partial pressure, P_{O2}. Free oxygen transport was governed by a reaction-convection-diffusion differential equation, shown in Eq. 19. Convective transport was driven by the steady-state velocity field, u, as described in Section 3.1.1.3. Diffusion was governed by the free oxygen diffusivity, D. A source term, φf, modelled oxygen transfer between the bound and free states within the blood cells, and a sink term, M, modelled metabolic clearance.

$$\frac{\partial c}{\partial t} + u \cdot \nabla c = D\nabla^2 c + \varphi f - M \quad \text{Eq. 19}$$

Both the free oxygen diffusivity, D, and solubility, α, varied between domains. As per Henry's Law (Eq. 20), this meant that, given a particular free oxygen concentration, the corresponding partial pressure was dependent on whether the oxygen was located in the vascular or interstitial domain.

$$P_{O2} = \frac{c}{\alpha} \quad \text{Eq. 20}$$

Haemoglobin-bound oxygen within the capillary was represented by the haemoglobin saturation, S, which related to the blood free oxygen partial pressure P_{O2RBC} via the Hill Equation (Eq. 21). The Hill exponent n and the half-maximal-saturation partial pressure, P_{S50}, are tabulated in Appendix 1. The molar concentration of haemoglobin-bound oxygen c_B, is linearly related to the saturation via the binding capacity of haemoglobin c_{Hb} (Eq. 22). Bound oxygen was only modelled in the vascular domain, with transport governed by a reaction-convection-diffusion differential equation (Eq. 23). Convection of bound oxygen occurred using the same velocity field u as for free oxygen, but the diffusive transport was dependent on the haemoglobin diffusivity, D_{Hb}.

$$S = \frac{P_{O2RBC}^n}{P_{O2RBC}^n + P_{S50}^n} \quad \text{Eq. 21}$$

$$c_B = c_{Hb} S \quad \text{Eq. 22}$$

$$\frac{\partial S}{\partial t} + u \cdot \nabla \mathrm{S} = D_{Hb}\nabla^2 S - f \quad \text{Eq. 23}$$

The transport of oxygen from the bound to free states within the blood cells was incorporated via a source/sink function, f (Eq. 24), from Clark et al. (1985). This function was set to zero in the interstitial domain. The parameter κ_{Hb} modelled the dissociation rate constant for oxyhaemoglobin (Eggleton et al. (2000)). The coefficient φ was then used to correct for the molar density of haemoglobin and is defined in Eq. 25 via the haemoglobin molar density N_{Hb}, the molar volume of oxygen at 36.9°C V_{molO2}, and a re-normalisation coefficient N_{50} from Clark et al. (1985).

$$f = \kappa_{Hb}\left(S - (1 - S)\left(\frac{P_{O2RBC}}{P_{S50}}\right)^{n}\right) \quad \text{Eq. 24}$$

$$\varphi = N_{50} N_{Hb} V_{molO2} \quad \text{Eq. 25}$$

Michaelis-Menten kinetics were used to model the metabolism of oxygen, M, within the interstitium (Eq. 26) (McGuire and Secomb (2001)). This only affected free oxygen within the interstitial domain, as M was set to zero within the capillary (Lucker et al. (2014)). This sink term was defined by the maximal oxygen consumption rate, M_0, the half-maximal-metabolism partial pressure P_{M50}, and the interstitial free oxygen partial pressure P_{O2int}. As P_{M50} was very small, the majority of oxygenated tissue was expected to be metabolised at the maximum rate.

$$M = \frac{M_0 P_{O2int}}{P_{O2int} + P_{M50}} \quad \text{Eq. 26}$$

Within the steady-state solver, the oxygen perfusion model was initialised at zero concentration c, and zero saturation S, at all locations except for the vascular inlet. Boundary conditions at the vascular inlet assumed a constant state of equilibrium between the free and

haemoglobin-bound oxygen. The steady-state free oxygen partial pressure at the inlet, P_{O2RBC0}, was set at a constant 90 mmHg (Lucker et al. (2014), Li et al. (2014), Welter et al. (2016)), to represent the blood oxygenation at the arterial end of the capillary. The free oxygen concentration boundary condition c_0 was set via Henry's Law, and the corresponding haemoglobin saturation boundary condition S_0 determined via the Hill Equation. All steady-state initial and boundary conditions can be found in Appendix 1.

3.1.1.2 Oxygen Bubble Deposition Model

As noted in the overview, following the computation of the steady-state oxygen distribution using the perfusion model a time-dependent solver step was added to model the transient effects of the nanobubbles. The steady-state oxygen distribution was used as the initial condition for the time-dependent solver. Within this solver, the boundary condition for the free oxygen concentration at the inlet to the capillary, c_0, was modified to incorporate the time-varying release of oxygen from the circulating nanobubbles, c_{NBO2} (Eq. 27).

$$c_0(t) = \alpha_{RBC} P_{O2RBC0} + c_{NBO2}(t) \quad \text{Eq. 27}$$

The concentration term c_{NBO2} was derived from the Oxygen Bubble Recirculation Model in Chapter 2. The time-varying molar depositions of bubble-oxygen in the tumour capillaries from each population, Δn_{O2TC} were combined and then scaled by the total volume of the tumour vasculature, V_{TC}, to generate the concentration profile used in the time-dependent solver (Eq. 28).

$$c_{NBO2}(t) = \frac{\sum_{pop} \Delta n_{O2TC}}{V_{TC}} \quad \text{Eq. 28}$$

Figure 10 shows a representative plot of c_{NBO2} for the case of the nanobubble population simulated in Chapter 2, using the experimental conditions from Owen et al. (2016) and Vasilyeva (2019).

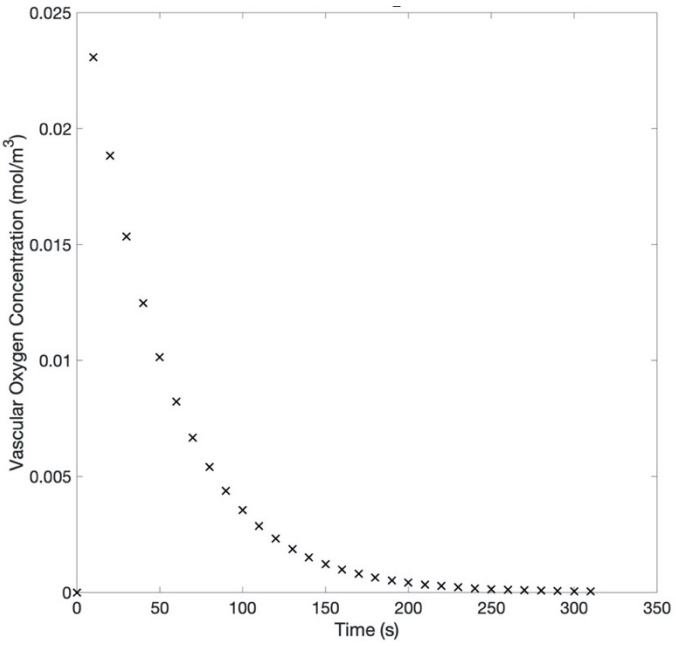


Figure 10. Concentration profile for the release of oxygen from circulating nanobubbles, c_{NBO2}, derived using results from the Oxygen Bubble Recirculation Model in Chapter 2.

For computational simplicity all of the bubble-released oxygen was assumed to remain in the free state prior to entering the capillary. Consequently, the S_0 boundary condition was unaffected by the bubble-oxygen release.

3.1.1.3 Fluid Mechanics Model

The fluid mechanics model was based on Arvanitis et al. (2018). The arterial-end capillary inlet was situated at the lowermost vascular boundary, and the venous-end capillary outlet at the uppermost vascular boundary. Fluid flow was therefore modelled in a positive y-direction (upwards) through the capillary. The velocity field, u, and hydrostatic pressure field, P, predicted by the fluid mechanics simulations were used to model the convective transport of oxygen.

As this model used a continuum approach to model the bloodstream, laminar flow was assumed for the vascular domain. This was modelled by the Stokes Equations (Eq. 29 - 30). As in Arvanitis et al. (2018), a hydrostatic pressure differential between the arterial and venous ends of the capillary, set at fixed pressures P_A and P_V respectively, was used to drive the flow. A no-slip boundary condition was used for the vascular wall. The resulting velocity profile in the capillary, and thus the volume flow rate of blood, was validated by comparison with murine *in vivo* experimental data from Unekawa et al. (2010).

$$\nabla P = \nabla\mu(\nabla u + (\nabla u)^T) \quad \text{Eq. 29}$$

$$\nabla \cdot u = 0 \quad \text{Eq. 30}$$

The Brinkman Equation for porous media flow (Eq. 31) governed fluid transport in the interstitium, with influx J_f defined by the hydrostatic pressure difference across the vascular wall, $\Delta P|_{Wall}$, and the hydraulic conductivity L_p (Eq. 32). Interstitial porosity ε_{int} and permeability k_{int} were parametrised as in Arvanitis et al. (2018), and the dynamic viscosity μ was assumed to be unchanged from the vascular domain as in the source paper. A symmetrical (zero normal flux) boundary condition was used at non-vascular interstitial boundaries, and the interstitial hydrostatic pressure was initialised at P_0 (Appendix 1).

$$\nabla P = \frac{\mu}{k_{int}} u - \frac{\mu}{\varepsilon_{int}} \nabla^2 u \quad \text{Eq. 31}$$

$$J_f = L_p * \Delta P|_{Wall} \quad \text{Eq. 32}$$

3.1.1.4 Single Capillary Geometric Model

For computational simplicity a single linear capillary was modelled in this part of the study (Figure 11). Experimental data from Unekawa et al. (2010) was used to set the length of the capillary, L, at 600 µm. The capillary diameter, d, was set at 5 µm as defined by Parpaleix et al. (2013) - this study was later used for validation of the perfusion model. The total width of the computational model, W, was set at 500 µm by an upper bound for capillary spacing in tumour tissue (Awwad et al. (1986)). The capillary was surrounded by an interstitial domain, with area A_{int} given by $L(W - d)$. Six geometric cut-lines were used for analyses. A longitudinal cut-line was located along the centreline of the vascular domain and ran the whole length of the capillary. Five transverse cut-lines were located perpendicular to the capillary between the vascular wall and the edge of the interstitium and were spaced by 137.5 µm. The computational mesh for the vascular domain was defined manually in COMSOL Multiphysics, with a maximum element size of 1 µm and minimum element size of 0.01 µm, and used a two-element boundary layer mesh along the internal capillary walls. The interstitial mesh was set using the pre-defined "Extremely Fine" mesh settings.

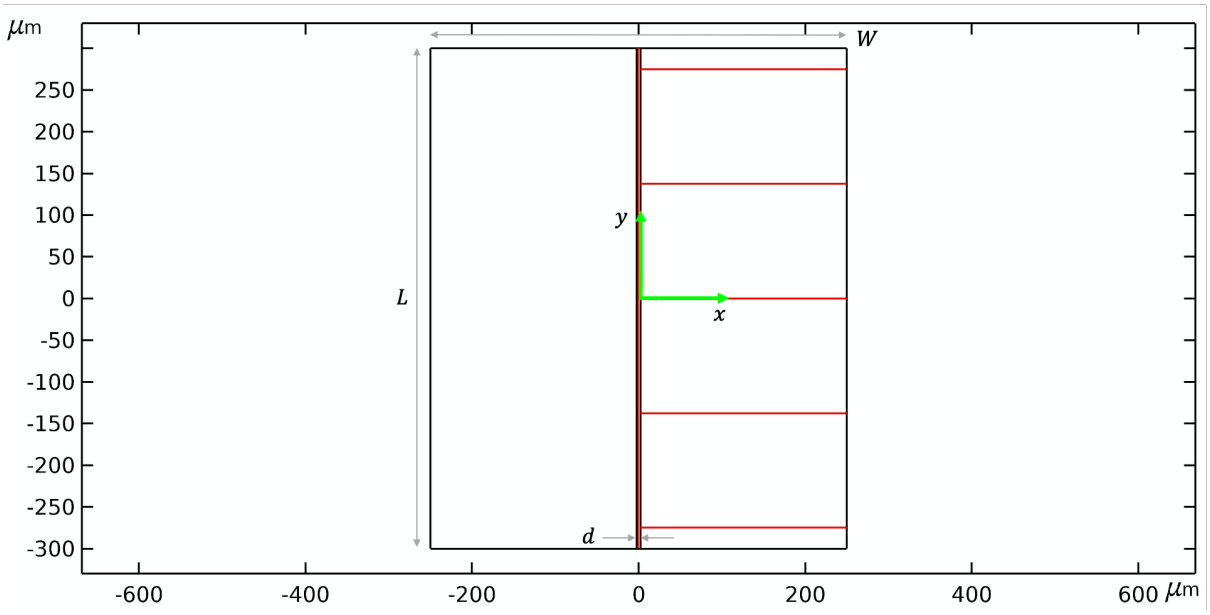


Figure 11. Single capillary geometry, displaying the transverse and longitudinal cut-lines (red), axes (green), and dimensions (grey).

3.1.1.5 Single Capillary Model Analyses

3.1.1.5.1 Validation of Model

The Oxygen Perfusion Model was experimentally validated by analysing the steady-state axial concentration gradient of free oxygen within the vascular environment. Parapaleix et al. (2013) investigated Erythrocyte-Associated Transients in capillaries using two-photon phosphorescence lifetime microscopy. Within this study, the authors evaluated the average free oxygen partial pressure, P_{O2exp}, at two points spaced ΔL apart within single capillaries. These experimental data were converted to a concentration gradient term (Eq. 33), with the spacing ΔL set at 49.7 μm (Parapaleix et al. 2013). This was compared to the axial concentration gradient $\frac{\partial c}{\partial y}$ predicted by the Oxygen Perfusion Model, measured along the longitudinal cut-line. Metabolic parameters for healthy tissue were used to generate the model data used in the comparison (Li et al. 2014).

$$\left(\frac{\partial c}{\partial y}\right)_{exp} \equiv \alpha_{RBC} * \frac{\Delta P_{O2exp}}{\Delta L} \qquad \text{Eq. 33}$$

It was important to compare the predicted vascular and interstitial oxygen distributions in tumour tissue versus healthy tissue, as only the latter case could be experimentally validated via Parapaleix et al. (2013). In this study, the only difference between the tumour and healthy tissue models was the Maximal Oxygen Consumption Rate, M_0, tabulated in Li et al. (2014) via Baxley and Hellums (1983).

3.1.1.5.2 Parametric Sensitivity Analysis

In order to ascertain the robustness of this oxygen transport model to uncertainties in its underlying parameters, a sensitivity study was conducted. Two metrics were defined to quantify the oxygen delivery predicted by the model (Eq. 34 – 35). The first metric, AF_H, was defined as the areal proportion of the interstitium oxygenated above a hypoxic threshold, set at 5 mmHg (0.00765 mol/m^3). The second metric, AF_N, was defined as the areal proportion of the interstitium oxygenated above a normoxic threshold, set at 50 mmHg (0.0765 mol/m^3).

$$AF_H = \frac{\int_{int}\left(\frac{c}{\alpha_{int}} > 5\ mmHg\right)\ dA}{A_{int}} \quad \text{Eq. 34}$$

$$AF_N = \frac{\int_{int}\left(\frac{c}{\alpha_{int}} > 50\ mmHg\right)\ dA}{A_{int}} \quad \text{Eq. 35}$$

The parametric sensitivity metric PSM was defined as the variation in AF_H produced by a change in a particular parameter, relative to its base value (Eq. 36).

$$PSM = \frac{AF_{H\pm 25\%} - AF_{H\,base}}{AF_{H\,base}} \quad \text{Eq. 36}$$

First, the response of AF_H to ± 25% variation in the following parameters was investigated: $c_{Hb},\ D_{int},\ D_{RBC},\ \alpha_{int},\ \alpha_{RBC},\ M_{0T},\ P_{M50},\ P_{S50},\ n,\ P_{O2RBC0},\ P_A,\ K,\ \varepsilon_{int},\ k_{int},\ L,\ W, d$. The area fraction AF_H was evaluated at the point of maximal bubble-oxygen deposition, defined as the point at which the surface integral of the free oxygen concentration c was at its highest. Thereafter, three parameters, $D_{RBC},\ M_{0T}$ and P_{O2RBC0}, were varied by more than 25% as part of the studies in the following sections.

3.1.1.5.3 Investigating Bubble-Enhanced Oxygen Diffusivity

In addition to oxygen bubble recirculation there is another mechanism hypothesised to account for the heightened oxygen deposition observed *in vivo*: the high oxygen solubility of the bubbles is thought to increase the effective diffusivity of free oxygen in the blood (Faithfull (1992)). To investigate this, the response of the area fraction AF_H to an increase in the free-oxygen diffusivity in blood, D_{RBC}, was studied. Within the time-dependent solver, D_{RBC} was increased by +25% to +100% and AF_H data were plotted in response. The variation in blood free-oxygen content, P_{O2RBC}, measured along the longitudinal cut-line, was also shown. Both AF_H and P_{O2RBC} data were evaluated at the point of maximal oxygen deposition.

3.1.1.5.4 Sensitivity of Deposition to Tumour Metabolism

In modelling metabolism, the maximal oxygen consumption rate, M_0, was reported as an order of magnitude greater in tumour tissue versus healthy tissue (Li et al. (2014), Baxley and Hellums (1983)). As metabolic rate is influenced by various physiological factors not modelled in this study (Grimes et al. (2014)), it was important to assess the response of the model to changes in M_0. A range of values from 1 - 100% of M_{0T} were trialled, and AF_H and AF_N data were produced both at the steady state and the point of maximal oxygen deposition.

3.1.1.5.5 Sensitivity of Deposition to Capillary Inlet Oxygenation

As the vascular network in tumour capillaries is highly irregular, the blood-oxygen levels, and thus, boundary conditions for the perfusion model, can vary significantly (Goldman (2008)). Therefore, the response of the single-capillary model to variations in the steady-state boundary partial pressure P_{O2RBC0} (and corresponding S_0) was investigated. P_{O2RBC0} was varied between 0 – 100 mmHg, and the response of the model was measured using the area fraction AF_H evaluated at the steady state and at the point of maximal oxygen deposition.

3.1.2 Results and Discussion

3.1.2.1 Fluid Mechanics Model

The hydrostatic pressure field and interstitial fluid velocity distributions are displayed in Figures 12 and 13. At the lowermost capillary boundary, the arterial gauge pressure P_A was 15 mmHg higher than that at the venous end (Levenbrown and Costarino (2019)), resulting in a hydrostatic pressure field which decreased upwards through the capillary. As fluid influx J_f was governed by the pressure difference between the vascular and interstitial domains, the corresponding interstitial hydrostatic pressure followed the same general trend.

Heterogeneity in hydrostatic pressure drove fluid through the model. As laminar flow was used to model the vascular domain, the cross-sectional velocity followed a parabolic profile. The average velocity in the single capillary was 1.70 mm/s, which is comparable with experimental data reported in Unekawa et al. (2010). This was an important result as this average velocity determined the volume flow rate of blood to the capillary, and thus total oxygen delivery to the model.

As symmetrical (zero normal flux) boundary conditions were used on all non-vascular interstitial boundaries, the only sites for the influx or efflux of fluid from the model was at the capillary inlet and outlet respectively. Correspondingly, a symmetrical velocity field developed in the interstitium. Influx from the arterial end of the capillary, with higher hydrostatic pressure, was balanced by efflux at the venous end, whereupon the fluid was then transported out of the model space via the capillary outlet. Interstitial regions closest to the capillary walls had the highest fluid velocities due to the relatively high pressure gradients. Convective transport of oxygen was therefore expected to occur primarily in these regions.

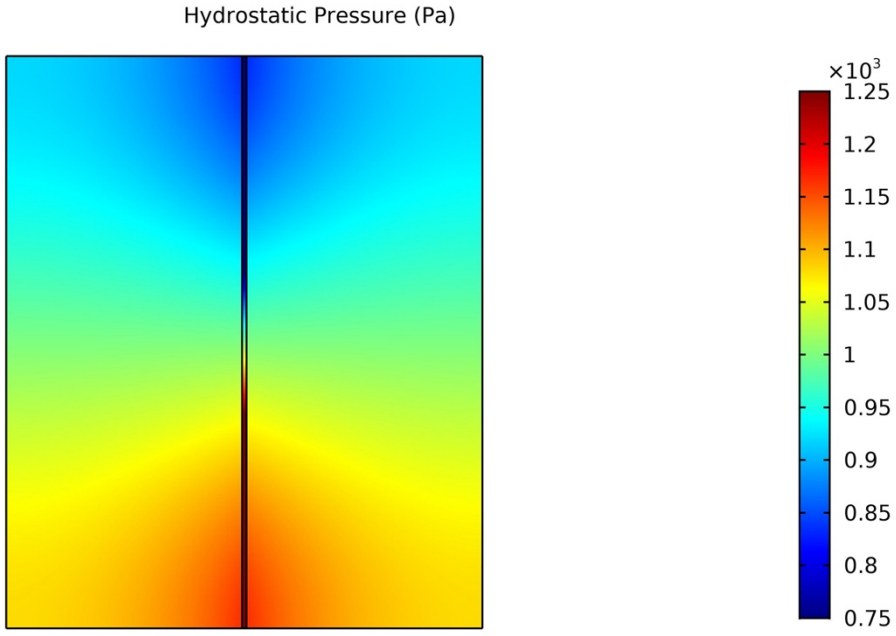


Figure 12. Hydrostatic pressure distribution in the vascular and interstitial domains, measured in Pascals. Vascular pressures exceed the ranges shown on the colourbar.

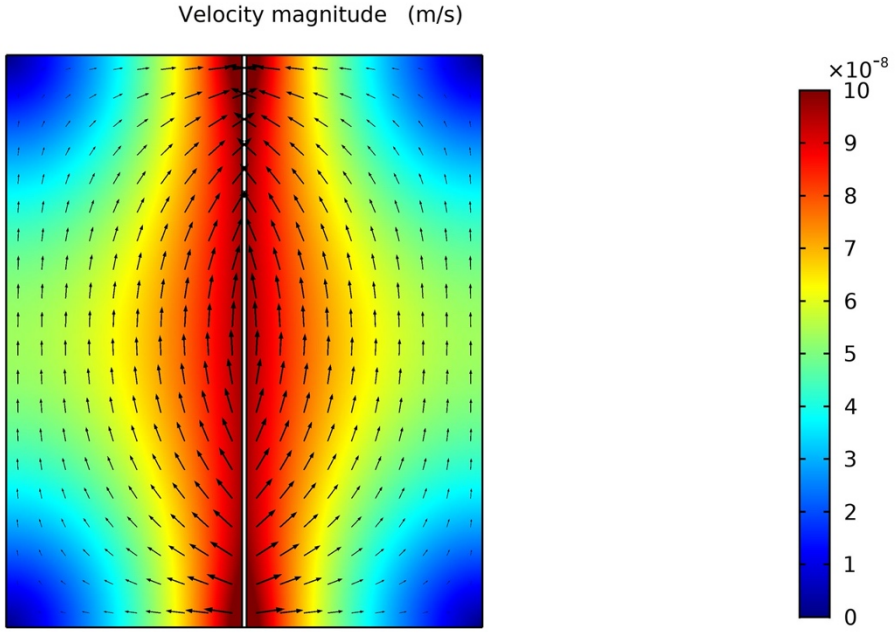


Figure 13. Interstitial fluid velocity field. A colour map shows the velocity magnitude in m/s and an arrow-field represents the direction of flow. Arrow lengths are proportional to the velocity magnitude.

3.1.2.2 Oxygen Perfusion Model

The steady-state distributions of free oxygen, generated using healthy and tumour tissue metabolic parameters, are shown in Figures 14 and 15 respectively. Colourbar ranges have been matched between the figures to aid comparison. Oxygen penetration was defined as the lateral distance from the capillary wall at which the free oxygen concentration equalled the hypoxic threshold value (5 mmHg).

Oxygen deposition was significantly higher throughout the interstitium for healthy tissue, as expected due to the order-of-magnitude difference between the maximal metabolic rate parameters. Even with the model width W, which modelled capillary separation, set using a neoplasm-derived value (Awwad et al. (1986)), the oxygenation of the healthy tissue interstitium exceeded 25 mmHg in all regions, indicating no areas of hypoxia.

In contrast, the oxygen supply to the tumour tissue was completely exhausted within 500 μm of the capillary inlet. At the steady state, the hypoxic-threshold area fraction AF_H was 15.9%. The corresponding normoxic-threshold area fraction AF_N was only 0.5%. Additionally, the maximum oxygen penetration within tumour tissue was 150 μm, signifying that hypoxia existed even in the interstitial regions closest to the capillary inlet, where deposition was highest.

In both cases, oxygen deposition was highest in the region close to the capillary entrance, and the interstitial oxygen concentration decreased along the capillary as a consequence of the reduced concentration gradient between the vessel and surrounding tissue. Additionally, within the interstitial region close to the vascular inlet the oxygen distributions generally followed the direction of highest lateral fluid velocity (see Section 3.1.2.1). This highlighted

the importance of the convective term in Eq. 19. However, oxygen transport was dominated by diffusion, evidenced by the limited axial reach of the blood-oxygen. Consequently, the interstitial deposition of nanobubble-released oxygen was predicted to be influenced significantly by the steady-state oxygenation.

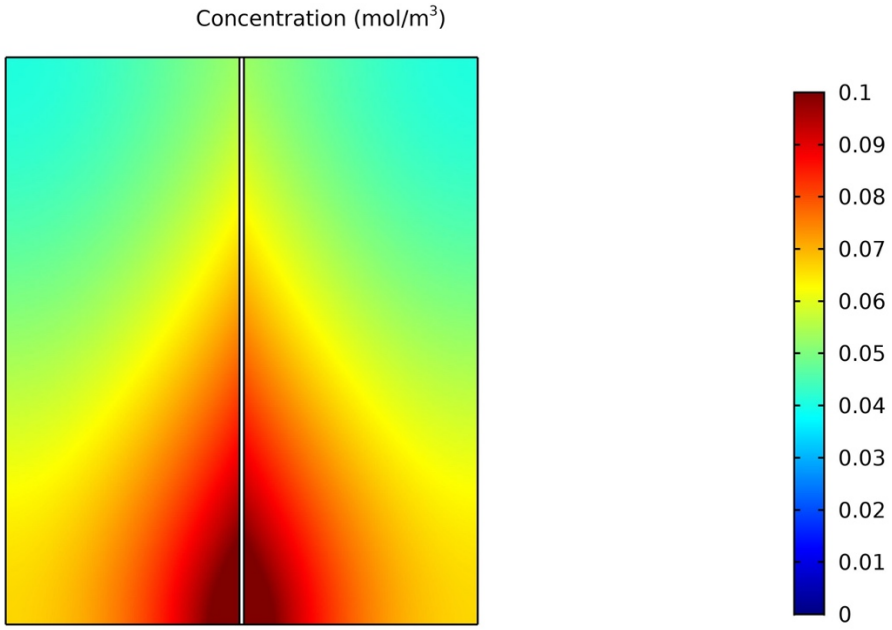


Figure 14. Steady-state free oxygen distribution evaluated using metabolic parameters for healthy tissue.

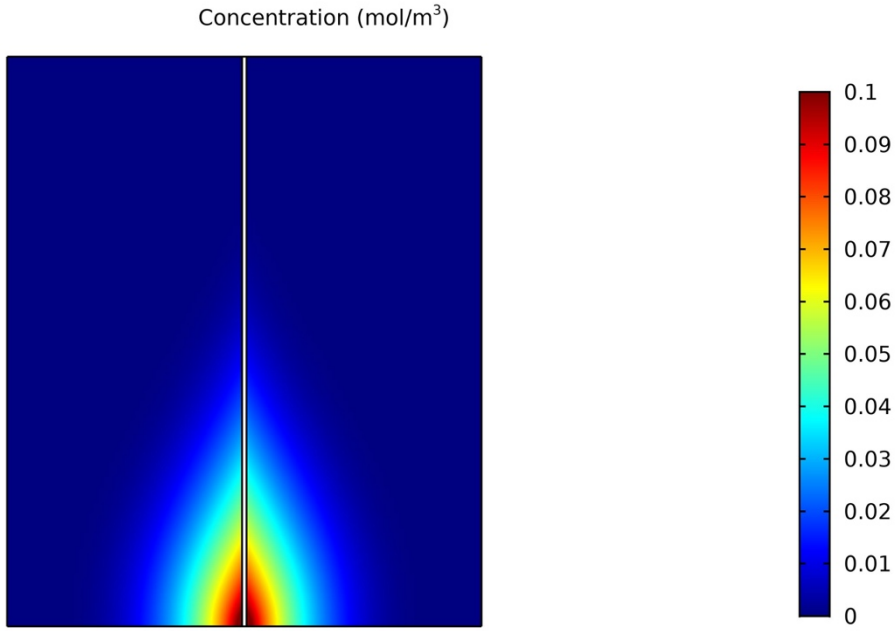


Figure 15. Steady-state free oxygen distribution evaluated using metabolic parameters for tumour tissue.

3.1.2.3 Oxygen-Bubble Deposition Model

By inspection of Figure 16, at the maximal bubble-oxygen deposition point, defined as the time when the surface integral of the free oxygen concentration c was at its highest, the general distribution of the nanobubble-released oxygen followed that of the steady-state oxygenation arising from perfusion. Regions with the highest deposition were situated close to the capillary entrance, with both deposition and penetration decreasing up the capillary. Oxygen deposition within the capillary fell to zero approximately 500 μm from the vascular inlet, which supported the conclusion of diffusion-limited transport.

The maximal bubble-oxygen deposition point occurred at t = 15s. The time lag between this maximal point and the maximum c_{NBO2} point (at t = 4.7s) was due to c_{NBO2} being incorporated using an inlet boundary condition. As oxygen convection was limited by the rate of blood flow, transport of the nanobubble-released oxygen throughout the rest of the capillary, and then the tissue, did not occur instantaneously.

The maximum interstitial deposition was 0.021 mol/m^3, which was approximately 15% of the highest steady-state oxygen level in the tissue. The hypoxic-threshold area fraction AF_H was 19.8% at the point of maximal deposition, an increase of 3.9 percentage points, or 25% relative to the steady-state value. The corresponding normoxic-threshold area fraction AF_N was 1.3%, an increase of 0.8 percentage points, or 160% relative to the steady-state value. These results suggest that the injected oxygen nanobubbles are capable of transiently generating a notable increase in oxygenation relative to the steady-state distribution. However, only a limited overall response is observed as the steady-state perfusion was only capable of oxygenating a small proportion of the tumour tissue.

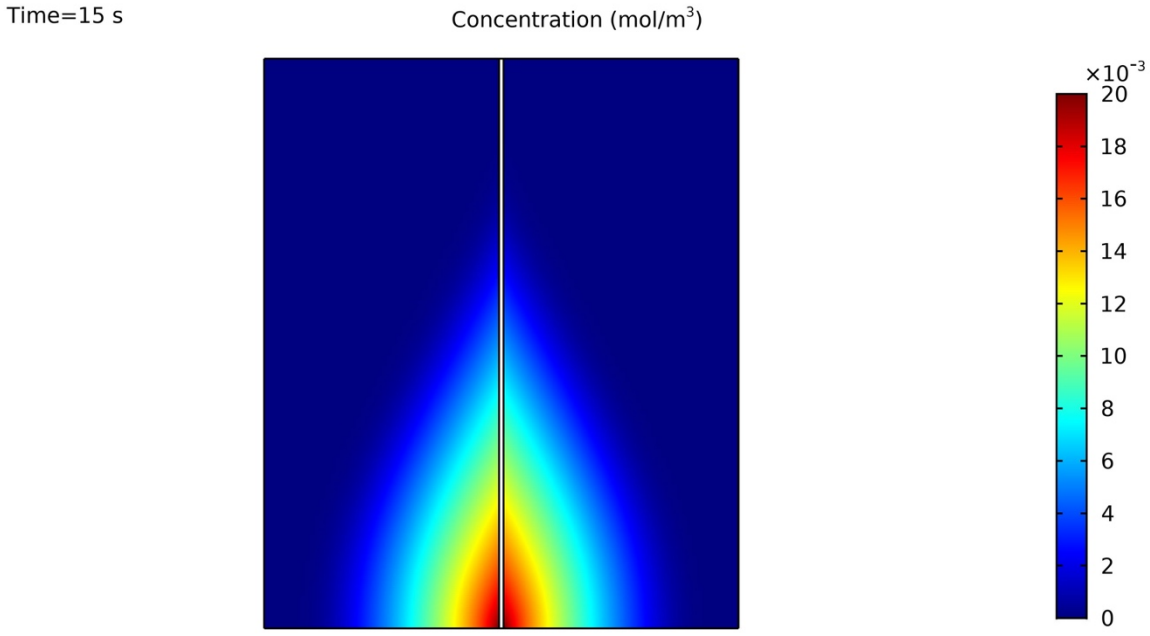


Figure 16. Deposition of bubble-released oxygen in tumour tissue, calculated via the difference between the free oxygen distributions measured at steady-state and at the point of maximal bubble-oxygen deposition.

Blood-oxygen data measured along the longitudinal cut-line is shown in Figure 17. The effect of bubble-released oxygen is clearly visible from the difference between the data evaluated at the maximal point (with bubbles) versus at the steady state (without bubbles). As expected, P_{O2RBC} and S were consistently higher at the maximal point. The difference between the P_{O2RBC} datasets was largest at the capillary inlet (~ 15 mmHg), and steadily decreased along the length of the capillary. At 300 μm from the inlet the difference had fallen < 5 mmHg.

In contrast, the largest difference in S (14.2%) occurred 200 μm from the capillary inlet. This was expected as the bubble-released oxygen term c_{NBO2} only modified the free-oxygen boundary concentration c_0; the boundary condition for haemoglobin-bound oxygen, S_0, was unchanged. Consequently, the heightened P_{O2RBC} caused the vascular saturation S to transiently rise up to 95.0% at 7.5 μm from the capillary inlet. After 7.5 μm, the nanobubble-enhanced S began to decrease on account of oxygen efflux to the surrounding tissue, and the

locus again followed the characteristic sigmoidal shape due to the Hill Equation (Eq. 21). The additional oxygen contributed to a shifting of the 50%-saturation point by 35 µm downstream, which represented ~6% of the total capillary length.

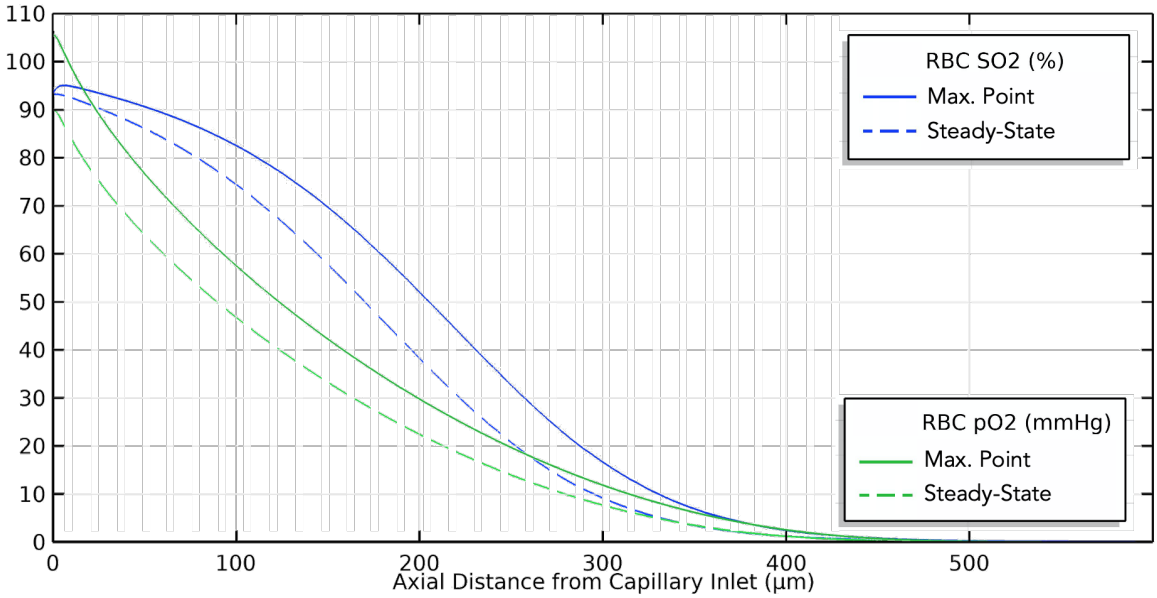


Figure 17. Oxygen-haemoglobin saturation (blue) and free oxygen partial pressure (green), measured along the longitudinal cut-line at the steady state (dashed) and at the point of maximal bubble-oxygen deposition (unbroken line).

Interstitial oxygenation measured along the transverse cut-lines is displayed in Figure 18. Data were evaluated both at the steady-state and maximal points for comparison. Oxygen penetration, defined via the hypoxic threshold, was notably increased by the addition of bubble-released oxygen to the system. At the cut-line 25 µm from the lower interstitial boundary (data shown in green), the hypoxic (5 mmHg) threshold position was shifted outwards by 12%, from 125 µm to 140 µm. At the mid-point of the interstitium (data shown in blue), the hypoxic threshold was shifted outwards by 185%, from 7 µm to 27 µm. The greater influence in the latter case is attributed to the lower steady-state oxygenation in this region providing a smaller resistance to diffusive transport of the bubble-released oxygen.

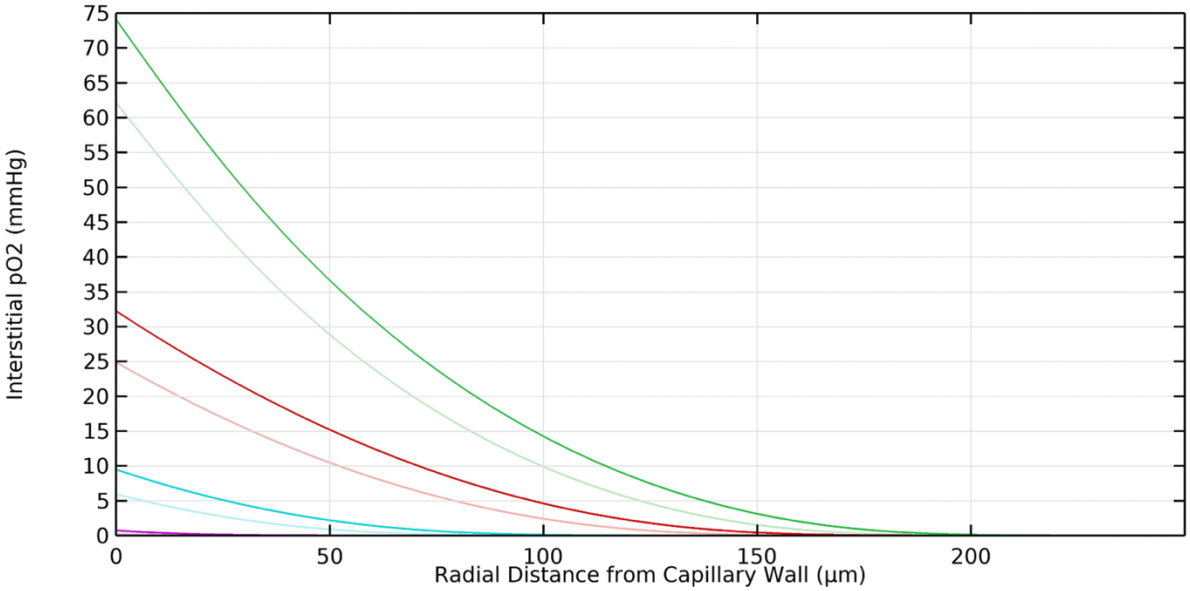


Figure 18. Interstitial free oxygen partial pressure, P_{O2int}, measured along the transverse cut-lines (Figure 11). Data were evaluated at the point of maximal deposition (bright colours) and at the steady-state (faded colours). The following colour scheme was used to delineate between the datasets: green – 25 µm / red – 162.5 µm / blue – 300 µm / purple - 437.5 µm from capillary inlet.

The time-evolution of AF_H and AF_N within the single-capillary model is displayed in Figure 19. Initially, the area fractions rose sharply, with maxima occurring at t = 15s, corresponding to the point of maximal bubble oxygen deposition. Area fraction maxima were 19.8% and 1.3% for the hypoxic and normoxic-threshold data respectively.

From t = 15s to t = 150s, the area fractions decayed exponentially. For example, at t = 50s, 100s, and 150s, AF_H was 17.9%, 16.6%, and 16.1% respectively. Relative to the steady-state values, this represented an AF_H increase by 11%, 4% and 2%. The effect on AF_H of the additional oxygenation at t = 150s represented 6% of that at the maximum point. The transient nature of the bubble oxygen release term, c_{NBO2}, used in Eq. 27, therefore directly influenced the oxygenation observed in the tumour tissue. This underlined the importance of optimising the nanobubble properties and dosing regime in order to maximise therapeutic benefit.

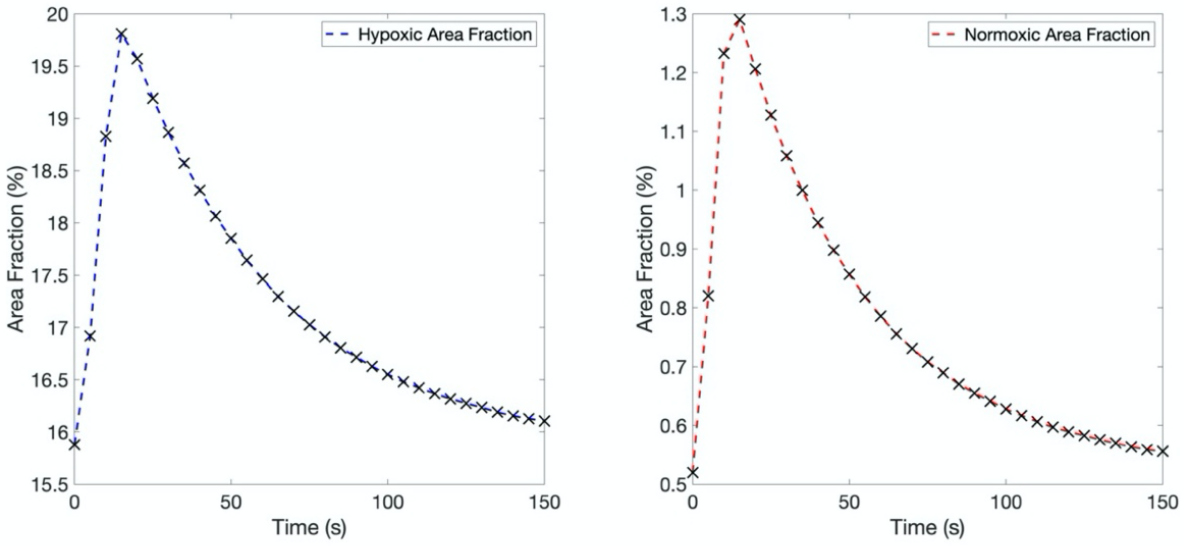


Figure 19. Time-evolution of the area fraction of interstitial tissue oxygenated above the hypoxic (left) and normoxic (right) thresholds of 5 mmHg and 50 mmHg respectively, following the injection of oxygen nanobubbles at t = 0 s.

3.1.2.4 Single-Capillary Model Analyses

3.1.2.4.1 Validation of Model

Figure 20 displays P_{O2RBC} and S as measured on the longitudinal cut-line, along the axis of the capillary, in both healthy and tumour tissue. Boundary conditions at the capillary inlet for P_{O2RBC} (90 mmHg) and S (93.3%) were identical for both cases.

For healthy tissue, P_{O2RBC} fell from 90 mmHg to 40 mmHg over the 600 μm length of the capillary. The venous-end blood oxygen level of 40 mmHg is very similar to the expected values reported in Guyton and Hall (2016). The axial free-oxygen concentration gradient was 111.6 ± 51.4 mol/m^4. This closely matched the 123.2 ± 64.3 mol/m^4 experimental data reported in Parpaleix et al. (2013).

Within tumour tissue, P_{O2RBC} and corresponding S fell to zero within 500 μm from the inlet, representing complete depletion of the capillary oxygen supply. Experimentally validating the tumour tissue concentration gradients was not possible. However, as parameter values used for the metabolic rates were reported in the same study, Baxley and Hellums (1983), validation using healthy tissue conditions was considered acceptable for overall validation of the perfusion model.

These results, coupled with the concordance between the fluid mechanical simulations and Unekawa et al. (2010), supported the use of this model for studying oxygen deposition.

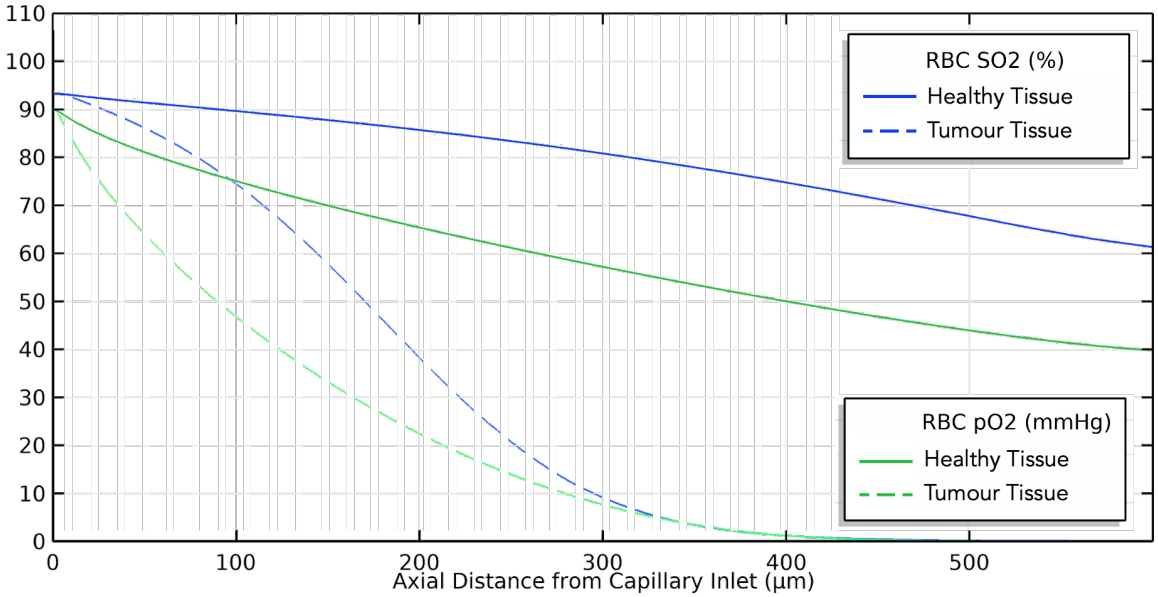


Figure 20. Steady-state oxygen-haemoglobin saturation (blue) and free oxygen partial pressure (green), measured along the longitudinal cut-line, using metabolic parameters for both tumour tissue (dashed) and healthy tissue (unbroken line).

3.1.2.4.2 Parametric Sensitivity Analysis

Figure 21 displays the response of the hypoxic-threshold area fraction, AF_H, to ± 25% variation in model parameters, evaluated at the point of maximal bubble-oxygen deposition. The sensitivity metric, PSM, is shown on the y-axis, and defined as the percentage change in AF_H from the baseline value (Eq. 36). Parameters with sensitivities under 0.1% were not shown in Figure 21.

Four parameters had a small (< 10%) effect on PSM: D_{int}, D_{RBC}, α_{int} and P_{M50}. Minimal sensitivity to D_{int} and D_{RBC} was observed, with PSMs of < 2% and < 0.2% respectively, suggesting that oxygen transport to the interstitium was relatively unaffected by uncertainty in the diffusive transport properties. Interestingly, an inverse sensitivity to D_{int} was found – higher interstitial diffusive transport slightly reduced the overall proportion of the interstitium above the hypoxic threshold - likely due to greater dispersal of the delivered oxygen

throughout the domain. Increasing α_{int} decreased the AF_H by a relatively small degree (-7.6%), with decreasing α_{int} having the opposite effect (+8.8%). As the hypoxic threshold value was a partial pressure term, this inverse relationship is explained by Henry's Law (Eq. 20). The half-maximal metabolism pressure P_{M50} had only a slight positive sensitivity. As P_{M50} was very low, the vast majority of oxygenated regions were metabolised at the maximal rate, and therefore ± 25% variation in its value generated only a small effect on AF_H.

Five parameters generated an intermediate effect (~20 – 30%): α_{RBC}, P_{O2RBC0}, P_A, W and M_{0T}. Linear, positive sensitivities were observed for α_{RBC}, P_{O2RBC0}, and P_A. Increasing α_{RBC} and P_{O2RBC0} increased AF_H as the free oxygen concentration was linearly related to these terms via Henry's Law. Arterial hydrostatic pressure P_A governed oxygen supply to the capillary, with fluid influx proportional to the pressure difference across the vascular domain. PSM was inversely related to the maximal metabolic rate M_{0T}, as increased metabolism caused greater clearance of oxygen from the interstitium.

Two parameters generated a large effect (> 50%): d and L. Increasing the capillary diameter d generated a very large positive increase in AF_H; as the fluid influx was pressure-driven, increasing the diameter massively increased the volume flow rate of oxygen into the vascular domain. Matching the vascular pressure difference to the capillary diameter was therefore critical to ensure the correct average velocity, and therefore oxygen supply to this model.

With regard to the other geometric factors, the large negative sensitivity of AF_H to the capillary length L, and capillary separation (via model width W), is immediately explainable by inspection of the pattern of oxygen distribution in Figure 15. Under tumour metabolic parameters, the entire vascular oxygen supply was exhausted at approximately 500 μm from

the inlet boundary. Increasing the total interstitial area therefore added additional hypoxic regions to the domain. As oxygen deposition decreased sharply downstream of the capillary inlet, increasing L contributed to a greater increase in hypoxic area compared to W.

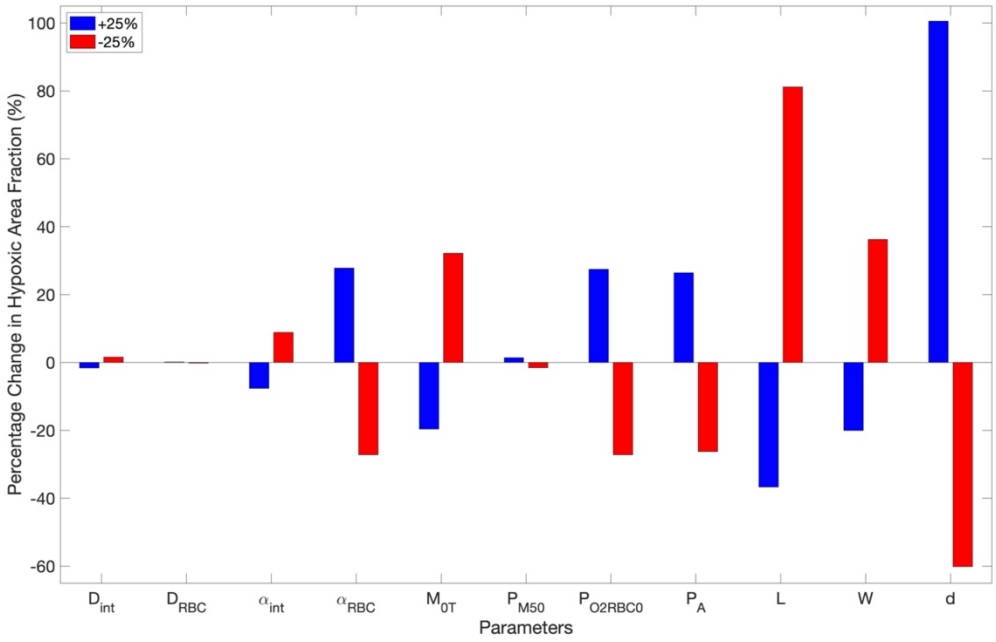


Figure 21. Parametric sensitivity analysis. Percentage variation in the hypoxic-threshold area fraction AF_H is plotted in response to ± 25% variation in the following parameters: interstitial diffusivity D_{int}, blood diffusivity D_{RBC}, interstitial solubility α_{int}, blood solubility α_{RBC}, maximum tumour tissue metabolic rate M_{0T}, half-maximal metabolic partial pressure P_{M50}, capillary inlet boundary oxygenation P_{O2RBC}, arterial gauge pressure P_A, vascular length L, model width W, and capillary diameter d.

3.1.2.4.3 Investigating Bubble-Enhanced Oxygen Diffusivity

The response of the model to variations in the blood free-oxygen diffusivity D_{RBC} is displayed in Figure 22 below. Hypoxic-threshold area fraction, AF_H, and blood oxygenation, P_{O2RBC}, data are shown. As D_{RBC} was only varied within the time-dependent solver, these data were evaluated at the point of maximal bubble-oxygen deposition.

As noted in the previous section, the baseline for the hypoxic-threshold area fraction, with unchanged D_{RBC}, was 19.8%. Whilst a general increase in area fraction was observed with increasing D_{RBC}, the magnitude of the increase was very small relative to the baseline value. As an example, if D_{RBC} was doubled, AF_H increased by ~0.12 percentage points, which is < 1% of the baseline value.

These results suggest that bubble-enhanced diffusivity only has a minimal impact on oxygen deposition from nanobubbles. The right-hand subplot in Figure 22 supports this analysis, as the difference in the rate of oxygen loss from the blood, characterised by the gradient of the P_{O2RBC} data, is imperceptible between the datasets.

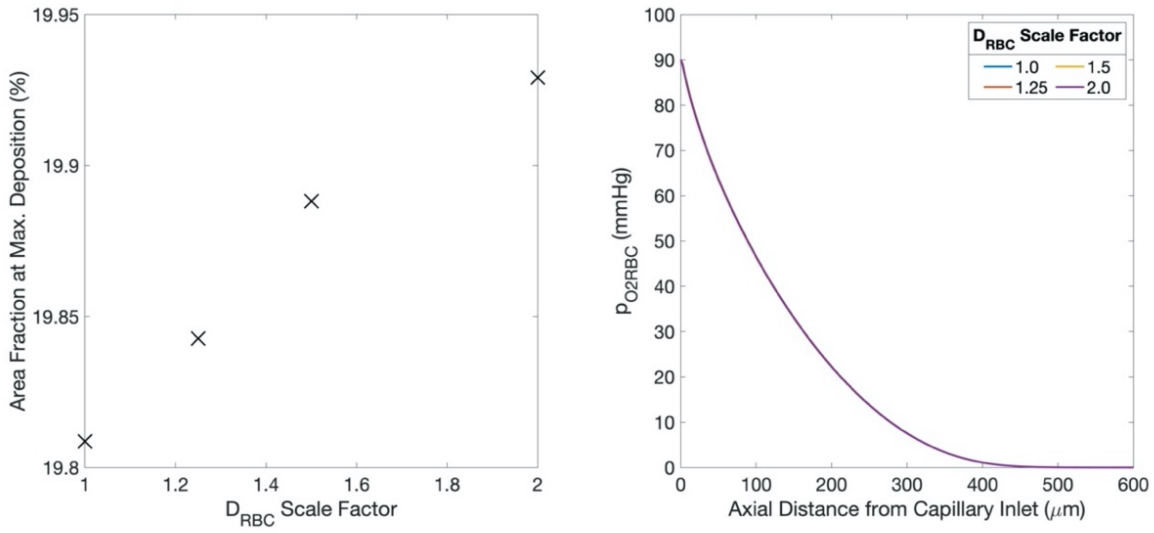


Figure 22. (Left) Hypoxic-threshold area fraction AF_H plotted in response to the D_{RBC} scale factor. (Right) Free-oxygen partial pressure variation along the longitudinal cut-line. Data generated using each of the D_{RBC} scale factors is shown.

Chapter 2 of this thesis concluded that recirculation of the injected oxygen nanobubbles is likely a crucial mechanism behind the heightened level of tumour oxygenation observed *in vivo* (Owen et al. (2016)). In contrast, the above analysis exploring the second hypothesis – that injected carriers increase the effective diffusivity of free oxygen in the blood – found that this mechanism contributes minimally to enhancing tumour oxygenation.

3.1.2.4.4 Sensitivity of Deposition to Tumour Metabolism

The response of the hypoxic- and normoxic-threshold area fractions, AF_H and AF_N, to variations in the maximal O_2 consumption rate for tumour tissue, M_{0T}, is shown in Figure 23. At very low M_{0T}, the deposition of oxygen from the blood occurred at a higher rate than the metabolic clearance of oxygen. This resulted in interstitial oxygenation above 50 mmHg (the normoxic threshold) in all areas and a corresponding initial plateau region with area fractions of 100%. As the rate of metabolism increased, the area fractions decreased with an inversely proportional relationship as less oxygen was available for transport.

As expected, the hypoxic threshold (5 mmHg) area fraction AF_H was higher than normoxic threshold AF_N (50 mmHg) data at all points bar the initial plateau region. Correspondingly, greater variability in the gradient, and therefore M_0-sensitivity, was observed for the normoxic-threshold dataset. Area fraction data evaluated at the point of maximal bubble-oxygen deposition was also consistently higher than steady-state data, as a result of the additional oxygenation provided by the nanobubbles.

Importantly for this study, the greatest sensitivity of this model to M_{0T} was observed between 10 - 25% and 25 - 50% of the literature value, using the hypoxic and normoxic thresholds

respectively. With ± 25% variation of the literature M_{0T} value, 0.0122 mol/m^{3}s, AF_H varied by < 1% using the hypoxic threshold, and < 10% using the normoxic threshold in both steady-state and maximal point data. This suggests that metabolic heterogeneity in the tumour interstitium is a relatively minor source of uncertainty within this model.

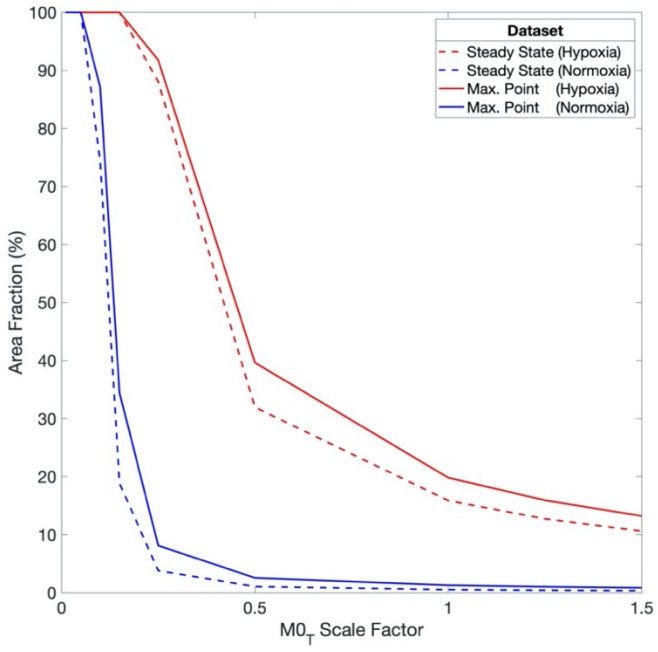


Figure 23. Hypoxic- (red) and normoxic-threshold (blue) area fraction variation in response to maximum oxygen metabolism rate M_{0T}, measured at the steady-state (dashed) and maximum point (unbroken line).

3.1.2.4.5 Sensitivity of Deposition to Capillary Inlet Oxygenation

Area fraction data generated using varying initial conditions for the inlet oxygenation, P_{O2RBC0}, is shown in Figure 24. Three AF_H curves are shown: steady-state (without nanobubbles), maximal-deposition point (with nanobubbles), and $AF_{H_{Dep}}$ (deposition due only to nanobubble-released oxygen, measured at the maximal-deposition point). $AF_{H_{Dep}}$ was calculated using the difference between the steady-state (blue) and the maximal point (red) AF_H datasets and had a baseline value of 3.9% using the 90 mmHg inlet condition.

Across the P_{O2RBC0} range of 0 – 100 mmHg, $AF_{H_{Dep}}$ varied from 0.6% to 4.0%. Within ± 10 mmHg variation from the 90 mmHg baseline, $AF_{H_{Dep}}$ varied by < 0.05 percentage points (or < 4% relative to the baseline value). Small perturbations in vascular oxygenation due to parametric uncertainty were therefore predicted to have a minimal effect on bubble-oxygen deposition.

Within deoxygenated capillaries, as P_{O2RBC0} was raised from 0 to 50 mmHg $AF_{H_{Dep}}$ increased from 0.6% to 3.6%. Higher blood-oxygen levels increase tissue oxygenation, and so with increasing P_{O2RBC0} the additional bubble-released oxygen was more likely to be sufficient to oxygenate above the threshold value. At ~32 mmHg, the effect of the nanobubbles was equal to that of the red blood cells. Above 50 mmHg, the effect of bubble-released oxygen only increased slightly, which is attributed to reduced steady-state concentration gradients near the inlet resulting in marginally increased deposition in low-oxygenation-areas further downstream.

As c_{NBO2} was unchanged, these results suggest that the influence of oxygen nanobubbles on the extent of hypoxia is significantly affected by blood-oxygen content when the capillaries

are deoxygenated. Neoplastic vasculature contains both oxygenated and deoxygenated capillaries, as perfusion is highly irregular (Breward et al. (2003)). Consequently, the final section in this thesis documents the investigation of nanobubble oxygen deposition using a heterogeneously perfused TME model.

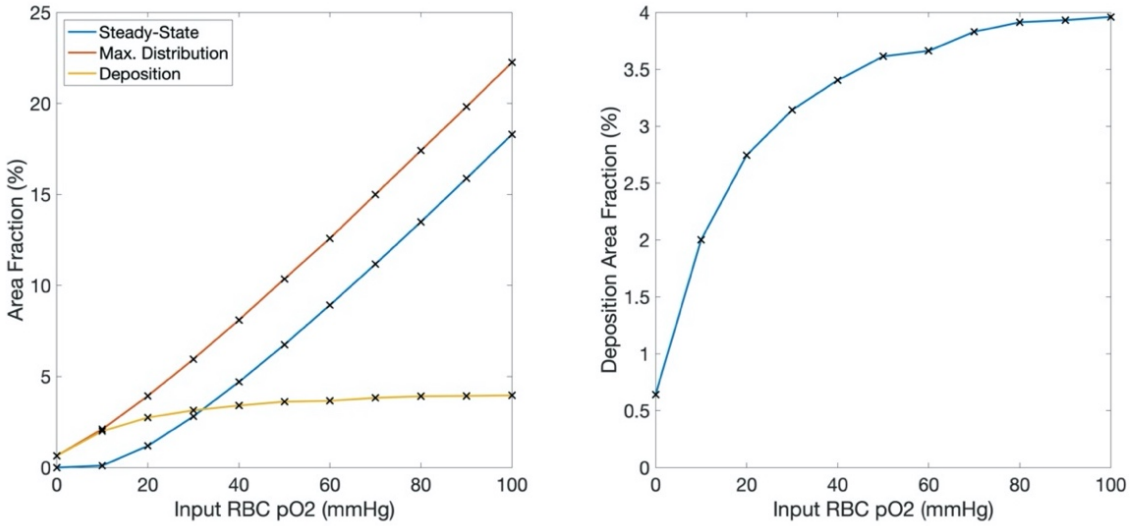


Figure 24. (Left) Hypoxic-threshold area fraction variation with capillary inlet partial pressure P_{O2RBC0}, measured at the steady-state (blue) and maximal depostion point (red). The area fraction due only to nanobubble-oxygen deposition was calculated using the difference between these two datasets. (Right) Magnified view of the bubble-deposition-only area fraction variation with P_{O2RBC0}.

3.2 Part 2: Oxygen Biodistribution in a Heterogeneously Perfused Tumour Microenvironment

3.2.1 Simulation Method

3.2.1.1 Overview and Percolation-Based Vascular Geometry

As noted previously, one of the primary causes of chronic hypoxia (along with heightened metabolism) is the irregular vasculature arising from abnormal angiogenesis within tumours (Shannon et al. (2003)). This results in a highly heterogenous microenvironment for oxygen delivery.

There are multiple approaches to modelling tumour capillaries, from simplistic single-vessel models to highly vascularised three-dimensional networks (Popel (1989), Goldman (2008)). For this two-dimensional study, a percolation-based capillary network model was used. A description of this approach, with experimental validation, can be found in Baish et al. (1996). The irregular vascular geometry model, shown in Figure 25, was a rescaled but otherwise identical version of that used in Arvantis et al. (2018); a description of the random-walk function used to formulate the geometry can be found in the Supplementary Information section.

Blood flow entered though a single vascular inlet at the lowermost capillary boundary, with width d. This boundary was initialised at oxygen concentration c_0, saturation S_0, and gauge pressure P_A. The five venous-end vascular outlets were set at P_V gauge pressure. Fluid flow would therefore predominantly occur in the positive y-direction (upwards). Values for these parameters were unchanged from single-capillary model (Appendix 1).

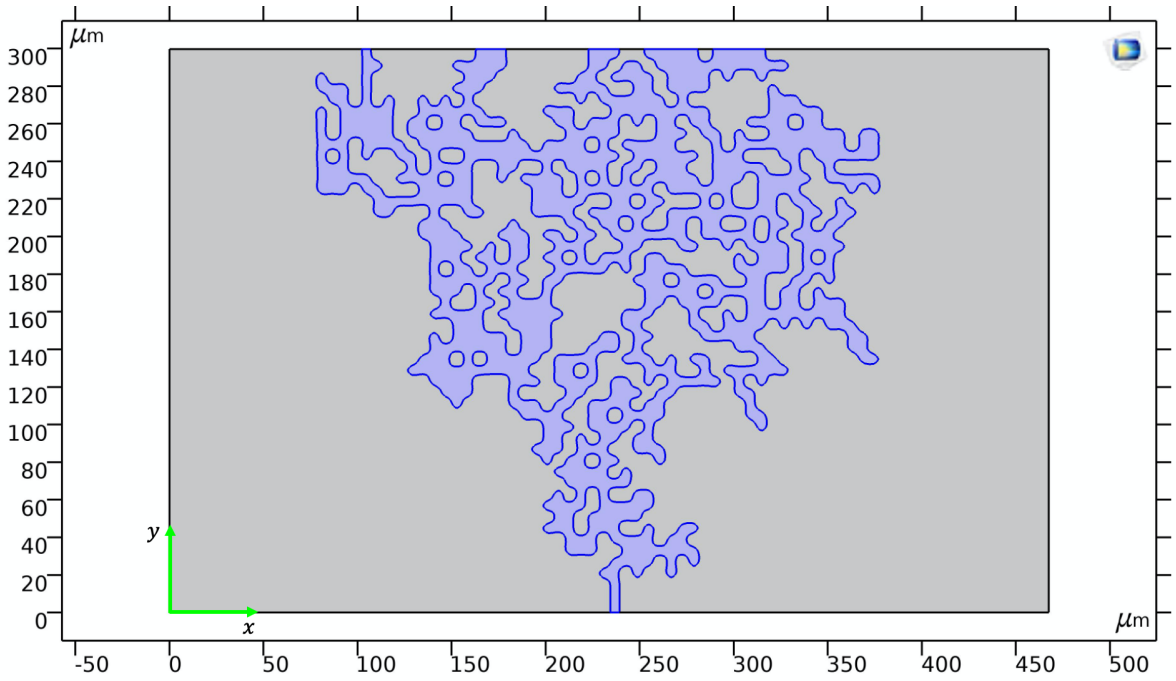


Figure 25. Irregular vasculature geometry model, with a single initial capillary inlet (lower boundary) developing into a complex vascular network with five outlets (upper boundaries). The vascular computational domain is highlighted (purple) to distinguish it from the surrounding interstitium (grey).

3.2.1.2 Analysis of Nanobubble-Released Oxygen Deposition

The complexity of the vascular network ensured multiple blood flow routes were possible within the geometric model. Results from the oxygen transport model were therefore analysed using the fluid velocity profiles for context; regions of the vasculature with limited blood flow would be deoxygenated relative to well-perfused capillaries and expected to deliver significantly less oxygen to the surrounding tissue. The steady-state oxygenation and distribution of nanobubble-released oxygen would therefore be spatially heterogenous within the interstitium and more reflective of neoplastic tissue compared to the single capillary model. Following the analysis of the fluid-mechanical and steady-state tissue oxygenation results, the spatial and temporal distributions of nanobubble-released oxygen were compared with the *in vivo* measurements reported in Owen et al. (2016).

3.2.2 Results and Discussion

3.2.2.1 Fluid Mechanics and Steady-State Vascular Oxygen Distribution

Hydrostatic pressure and velocity fields within the interstitium and vasculature are displayed in Figures 26 and 27. The highest interstitial fluid flux occurred at the outermost edges of the vascular network, in the direction and locations of greatest pressure difference. The overall fluid flow pattern in the interstitium was similar to the single capillary model: high interstitial influx at the arterial (lowermost) end of the network was counterbalanced by efflux back into the vasculature at the venous (uppermost) end.

Within the vascular network, Figures 28 and 29 display the velocity field u and the corresponding steady-state blood-oxygen level P_{O2RBC}. The vascular model represented a heterogenous network of multiple tumour capillaries. As a result, the total vascular area was significantly (37.5x) larger than in the single capillary model. As fluid velocity was driven by a fixed pressure difference between the single inlet (at P_A) and five outlets (at P_V), this resulted in a higher rate of perfusion. The mean fluid velocity in the straight capillary section closest to the network inlet was 7.6 mm/s, 4.5x greater than that from the single-capillary geometry and within 1 mm/s of the upper bound of velocities from Unekawa et al. (2010). By continuity, the rate of perfusion and therefore oxygen supply was 4.5x higher in the network model. In regions with increased capillary diameter, the velocity fell to maintain the mass flow rate.

Bifurcations in the network provided multiple routes for the blood flow; the primary route taken is highlighted by the highest velocities in Figure 28. With heterogeneity in vascular perfusion, the corresponding steady-state blood-oxygenation varied significantly throughout the capillary network (Figure 29). Along the primary blood flow path, P_{O2RBC} fell from 90

mmHg to 65 mmHg, rather than to 0 mmHg in the single-capillary geometry. Only a very small region of the vascular network, located on the upper-left of the model, was completely deoxygenated at the steady-state. This increased vascular oxygenation was attributed to higher blood flow and reduced efflux per μm of capillary length; each capillary section perfused a much smaller region of interstitium compared with the single-capillary model.

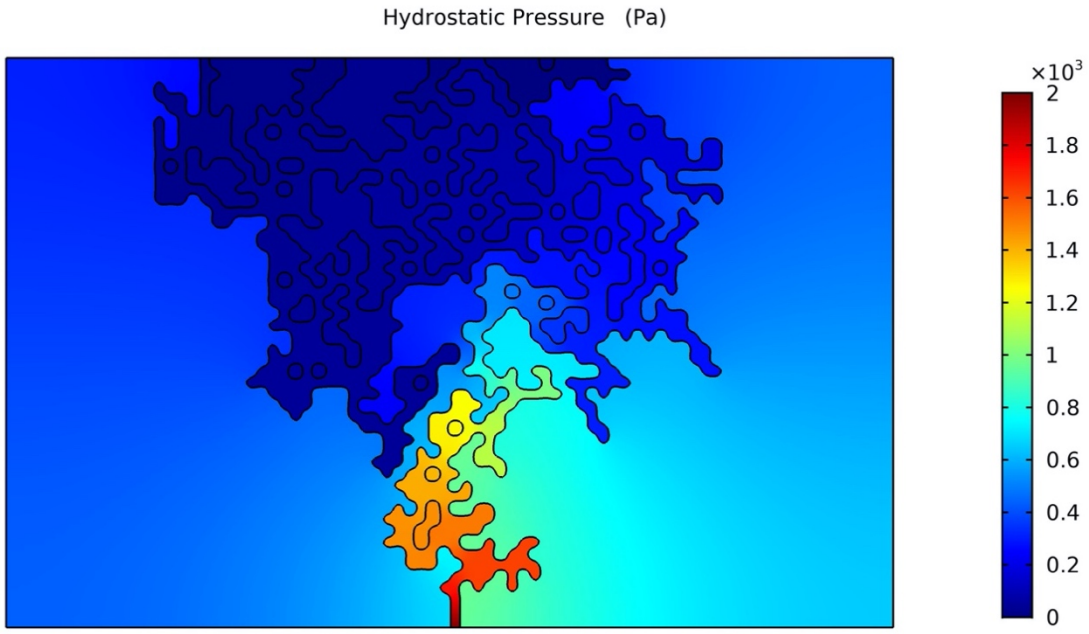


Figure 26. Hydrostatic pressure distribution in the vascular and interstitial domains, measured in Pascals.

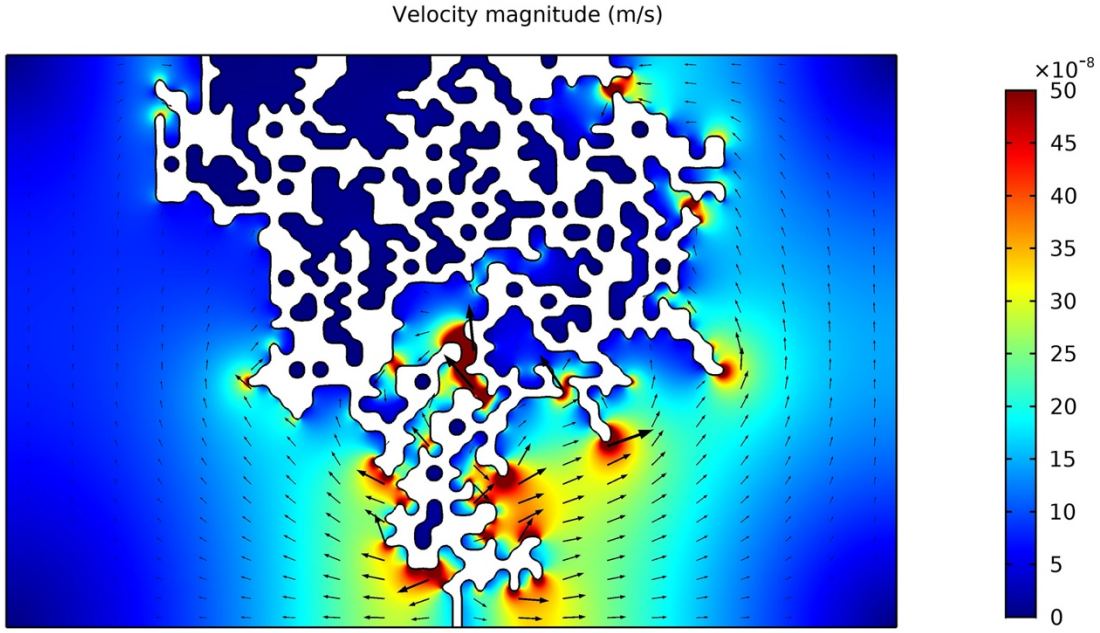


Figure 27. Interstitial fluid velocity field, comprising a colour plot of the velocity magnitude in m/s and an arrow-field representing the direction of flow. Arrow lengths are proportional to the velocity magnitude.

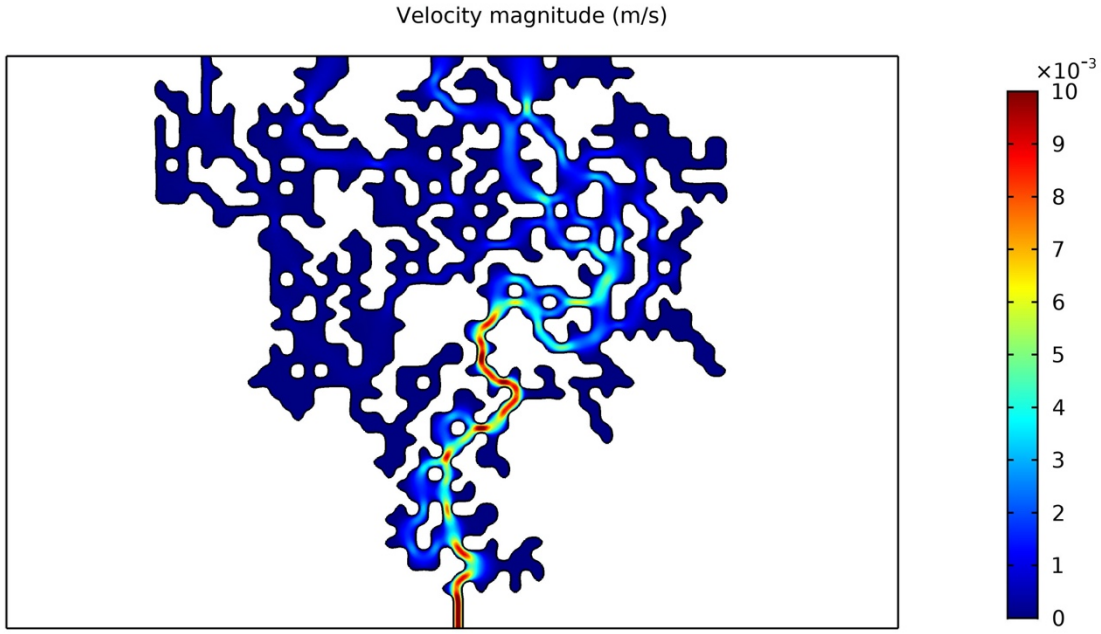


Figure 28. Velocity field u within the vascular network, measured in m/s. The heterogeneity in perfusion is clearly visible; the primary route taken by the blood was defined as the path with the highest fluid velocities.

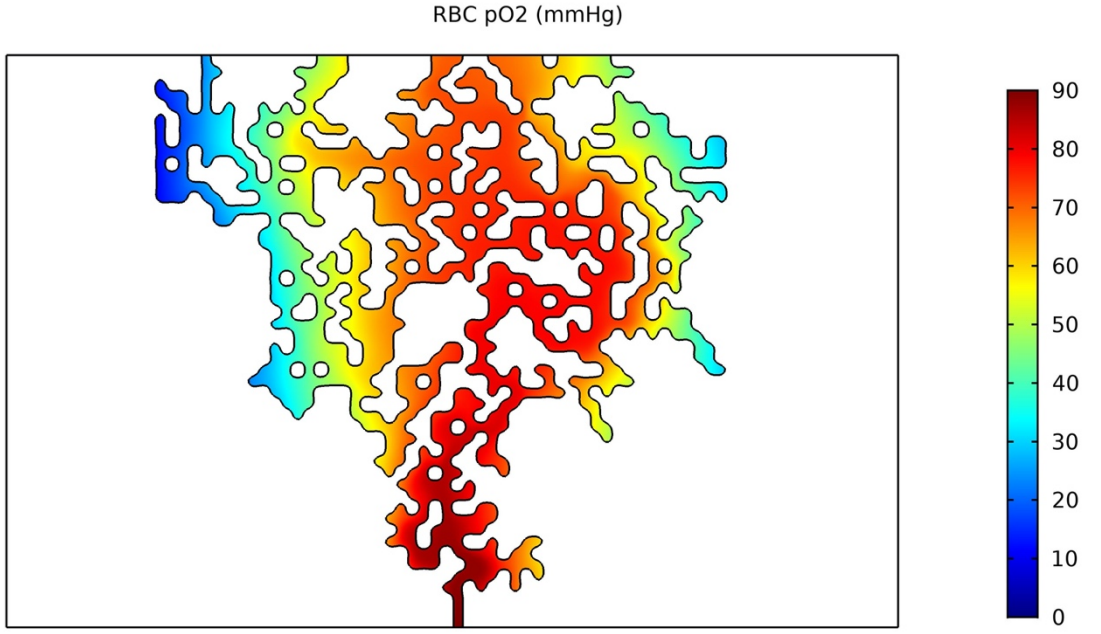


Figure 29. Steady-state distribution of free oxygen partial pressure, P_{O2RBC}, within the vasculature, measured in mmHg.

Consequently, the vascular model contained both highly oxygenated and deoxygenated blood vessels, allowing for analysis of the heterogeneity of nanobubble-released oxygen deposition within the tumour tissue.

3.2.2.2 Blood and Nanobubble-Released Oxygen Deposition in the Heterogeneously Perfused Tumour Microenvironment

The distribution of the free oxygen concentration c throughout the vascular network and the tumour interstitium is displayed in Figures 30 and 31. The data shown in Figure 30 were produced at the steady state, before any nanobubble deposition. The nanobubble-enhanced free oxygen distribution is included for visual comparison in Figure 31. As previously, when the nanobubbles were introduced the oxygen distribution varied in time, and the peak deposition (defined as the time when the surface integral of the free oxygen concentration was at its highest) occurred at t = 20s.

Inspection of both distributions highlights the heterogeneity in blood and nanobubble-released oxygen deposition. At the steady state, highly vascularised interstitial regions close to the primary blood flow route (see Figure 28) were oxygenated from 0.1 – 0.12 mol/m^3 (equivalent to 65 – 78 mmHg). These values were similar to the highest levels of oxygenation observed in the single-capillary model, suggesting that the increased rate of perfusion was sufficient to oxygenate the tissue in spite of the high tumour metabolism.

In contrast, the outermost sections of the vascular network received significantly less blood flow. Correspondingly, interstitial areas in close proximity to the vascular periphery were oxygenated between 0.02 – 0.06 mol/m^3 (equivalent to 13 – 39 mmHg). Oxygen levels at the outer boundaries of the interstitium, representing the points of maximal separation between microvascular networks, were the lowest observed in the model. On average, the left-hand boundary was oxygenated at 0.001 mol/m^3 (0.8 mmHg) and the right-hand boundary at 0.018 mol/m^3 (11.6 mmHg). The difference in boundary values was attributed to the asymmetrical network geometry and the primary route taken by the blood (Figure 28).

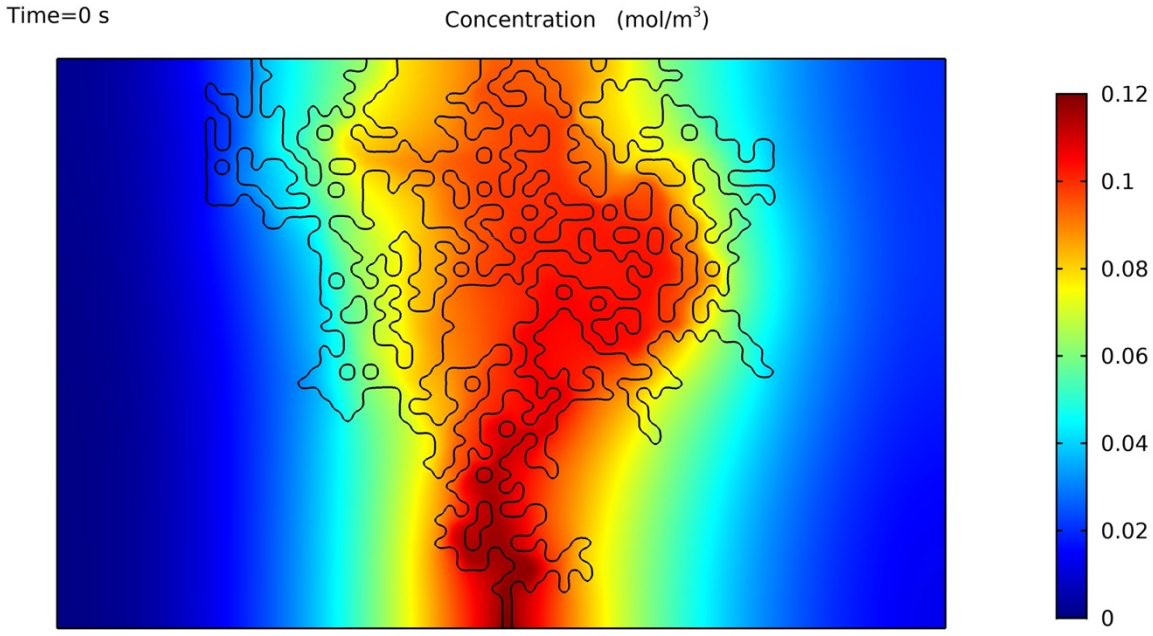


Figure 30. The free oxygen distribution in the vascular model, measured in mol/m^3 and evaluated at the steady state (prior to nanobubble injection).

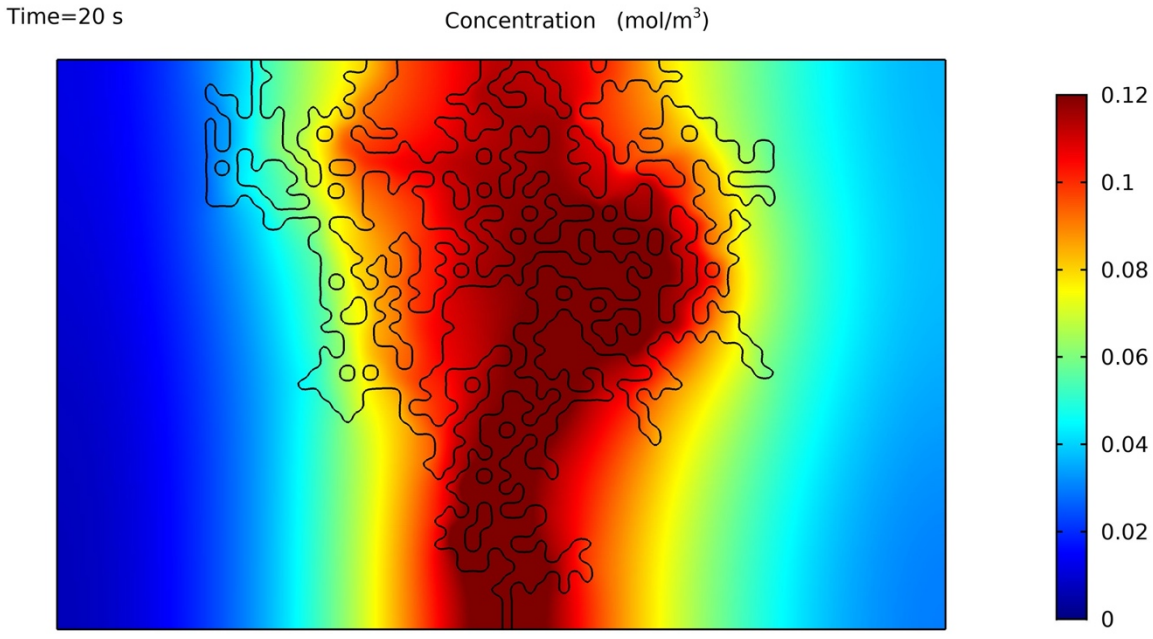


Figure 31. The free oxygen distribution in the vascular model, measured in mol/m^3 and evaluated at the point of maximal oxygen deposition (where the effect of the nanobubbles was the highest). This occurred 20s after intravenous injection of the bubbles.

As shown in Figure 32, the release of oxygen from the nanobubbles was spatially and temporally heterogeneous. Maximal deposition occurred along the primary blood flow path, with the additional oxygenation diminishing with increasing distance. Interstitial oxygenation was therefore highly asymmetric.

Increased vascular oxygenation due to nanobubble oxygen release gave rise to higher interstitial oxygen levels, with a time lag due to the non-instantaneous nature of diffusive and convective transport. The maximal points for the hypoxic- and normoxic-threshold area fractions, AF_H and AF_N, occurred at 17.5s and 22.5s respectively, both 2.5s (one timestep) apart from the surface-integral-defined maximum point. The AF_H maximum was reached first as the low hypoxic threshold required less additional vascular oxygen to generate sufficient deposition in the interstitium. Conversely, the AF_N threshold was higher than the mean tissue oxygenation, and therefore was reached after the maximal deposition point.

At the maximal bubble-oxygen deposition point (t = 20s), the concentration gradient between the vascular network and surrounding tissue had diminished markedly when compared to t = 15s. From t = 20s, the total oxygenation within the model began to decrease; exponential decay of the concentration levels can be observed from the plots at t = 50s, 100s, and 150s. These results therefore predict only a small window of significant bubble-enhanced tumour oxygenation, even within a highly vascularised computational model of the TME.

With regards to further substantiating the oxygen bubble recirculation hypothesis, the spatial distribution of nanobubble-released oxygen within the interstitium was compared to experimental data. As tabulated in Table 2 (Chapter 2), the *in vivo* oxygenation reported in Owen et al. (2016) was recorded at 600 ± 350 Pa (equivalent to 4.5 ± 2.6 mmHg) at t =

1800s using an oral suspension of nanobubbles. When converted to units of concentration, this represented bubble-oxygen deposition of $6.9 \pm 4.0 \times 10^{-3}$ mol/m^3 within the tumour interstitium. Inspection of Figure 32 highlights the agreement between these values and the simulated spatial distribution of nanobubble-released oxygen. Within the simulations, oxygen deposition above 1.9 mmHg, 4.5 mmHg, and 7.1 mmHg (the lower, middle, and upper bounds of the experimental data) was observed within the interstitium at up to t = 112.5s, 72.5s, and 52.5s respectively, which is ~20 times faster than reported experimentally. By t = 250s the deposition of bubble-released oxygen had diminished below detectable levels in the model. This rate of decay contrasts with the significantly higher longevity of the nanobubble oxygenation observed *in vivo*, which indicated elevated oxygen levels 30 minutes from the time of oral delivery.

Two mechanisms may explain this temporal disparity. When compared to intravenous injection, there would be expected to be a time lag between oral delivery and maximal interstitial deposition due to absorption of the nanobubbles in the gut. Modelling the oral pharmacokinetics was considered too parametrically uncertain for computationally testing the reoxygenation hypothesis, and so IV delivery was instead simulated. As discussed in Chapter 2, nanobubbles may also have a different physical structure to microbubbles, which enhances their stability. In both cases, the *in silico* timeframe for bubble-released oxygen deposition was likely under-predicted and further work would be needed to revise the model and/or perform further *in vivo* experiments.

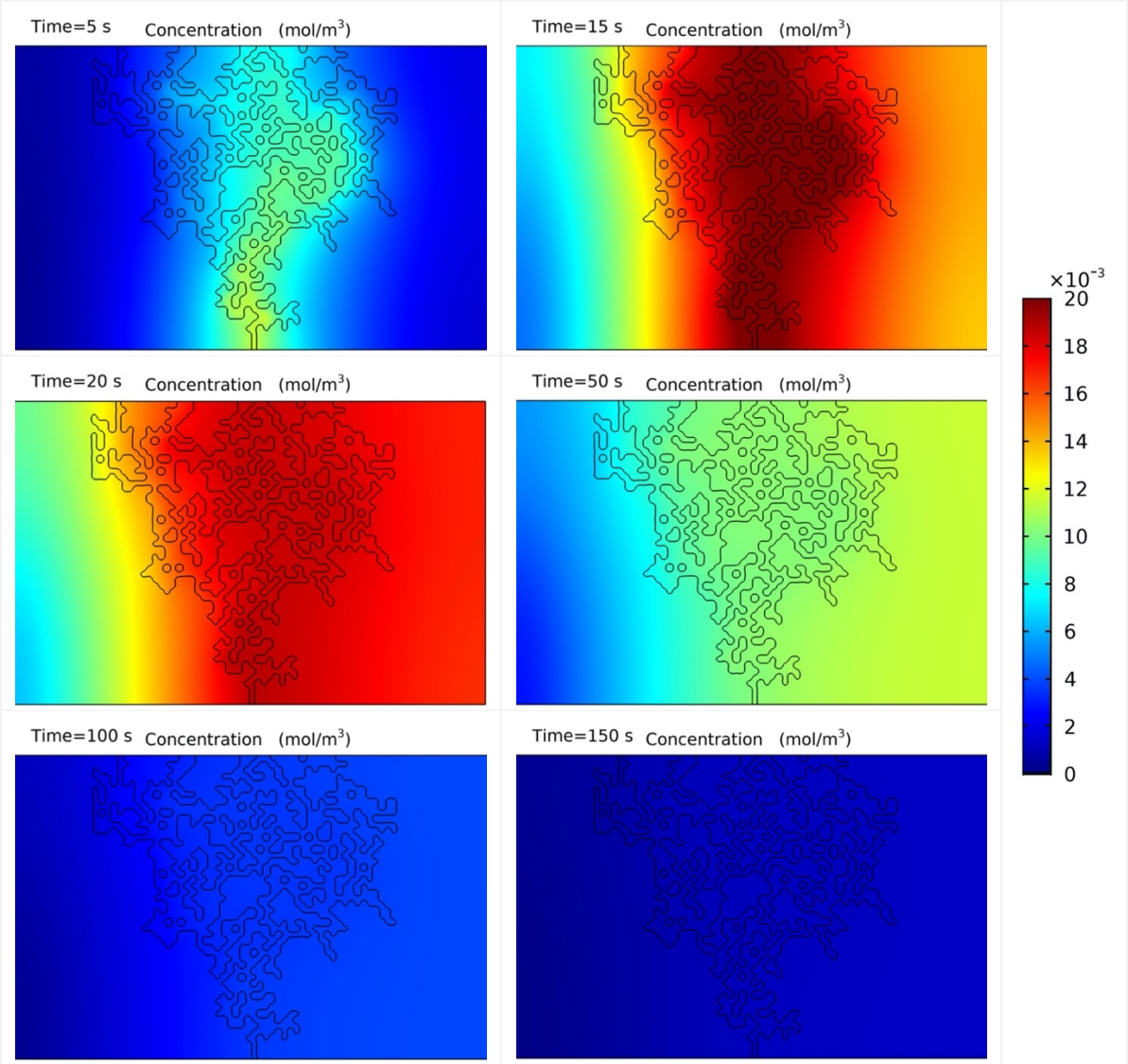


Figure 32. Deposition of bubble-released oxygen in tumour tissue, calculated via the difference between the free oxygen distributions measured at steady-state and at the various time points shown.

3.3 Part 3: Chapter Conclusions and Future Work

The *in silico* studies documented in this chapter generated predictions of the spatial and temporal distributions of blood- and nanobubble-released oxygen within a vascularised tumour microenvironment (TME) model.

Insight into oxygen transport was first gained using a single-capillary geometry for computational simplicity. A hypoxic-threshold area fraction metric, AF_H, was defined to evaluate the degree to which nanobubble-released oxygen alleviated tissue hypoxia. Results from this model were validated by comparison of the axial free oxygen concentration gradient within the capillary to analogous experimental data reported in Parpaleix et al. (2013). Bubble-enhanced oxygen diffusivity was observed to have a minimal effect on the level of oxygen deposition, suggesting that reoxygenation of the nanobubbles is a more important mechanism for oxygen delivery to the TME. Parametric sensitivity analyses elucidated the importance of the maximal metabolic rate in determining both the steady-state tissue oxygenation and the effect of nanobubble-released oxygen. High sensitivity of AF_H to the capillary inlet oxygenation was also observed, suggesting that the relative effect of bubble-oxygen deposition is reduced in deoxygenated capillaries. As tumour tissue is heterogenous and contains both oxygenated and deoxygenated vessels, these results supported further investigation using a more complex vascular geometry model.

The numerical model was then applied to a percolation-based vascular network geometry to evaluate the temporal and spatial heterogeneity of bubble-released oxygen deposition within the TME. At the point of maximal bubble-oxygen deposition, and for approximately two minutes following intravenous injection, the additional oxygenation was found to encompass the range of *in vivo* experimental data reported in Owen et al. (2016). Detailed comparison

between the simulated and experimental results was limited by the singular nature of the fibre-optic data (one data point per mouse) and the limited number of total data points (n = 8) in the experimental study. Following the publication of additional *in vivo* data in the literature, further analysis using this computational model should be undertaken.

Additionally, the simulation results predicted a transient response which decayed to zero within 250s. This contrasted with the oxygenation data in Owen et al. (2016), which reported elevated oxygen levels at 30+ minutes following oral delivery. The difference in timescales for the oxygen deposition was thought to be primarily due to two mechanisms: (i) the simulating IV injection of the nanobubbles negated the absorption pharmacokinetics in oral delivery and (ii) the use of microbubble physics to describe oxygen nanobubbles may have significantly underestimated the dissolution timeframe. Incorporation of nanobubble-specific modelling techniques and murine nanobubble pharmacokinetics within the TME model are therefore important areas for future work.

In order to maximise the clinical potential of oxygen-enhanced cancer therapy, further investigation of the pharmacokinetic/dynamic behaviour of both oxygen and the injected drug within the TME model is required. In particular, optimisation of the nanobubble properties and dosing regimen is required to maximise the adjuvant effect of the oxygenation, which will be specific to each therapeutic molecule.

In summary, this chapter extends the modelling reported in Chapter 2 by comparing the simulated distribution of nanobubble-released oxygen within the TME to *in vivo* experimental data reported in Owen et al. (2016). Whilst limited by the sparsity of the literature data, concordance between these results supported the computational approach used

within this study. Relative to the original research objectives, results from this chapter (i) provisionally supported the importance of nanobubble reoxygenation as a mechanism for oxygen deposition in tumour tissue and (ii) highlighted the importance of vascular heterogeneity on the capability of oxygen carriers to relieve tissue hypoxia.

4 Overall Conclusions to Study

In order to better understand the clinical potential of artificial oxygen carriers to alleviate tissue hypoxia, the mechanisms of oxygen deposition from injected nanobubbles to the hypoxic tumour microenvironment (TME) were studied *in silico*.

In Chapter 2, simulations recreating the *in vivo* experimental conditions in Owen et al. (2016) found that reoxygenation of injected oxygen nanobubbles was a significant contributor to tumour oxygenation, with over 90% of the total oxygen deposition within tumour tissue predicted to arise from reoxygenated nanobubbles. Additionally, the volume-averaged maximum oxygen deposition predicted within the TME (1240 Pa) was of a similar order to the experimentally observed oxygen deposition (600 ± 350 Pa) in Owen et al. (2016). The total oxygen deposition in the tumour was found be highly sensitive to bubble size and concentration and to tumour volume and vascularity. The simulations also indicated that higher levels of oxygen deposition could be achieved with the initial injection by changing the administration regime from intravenous (IV) to intra-arterial (IA).

The models in Chapter 2 assumed (i) a homogenous distribution of nanobubble-delivered oxygen and (ii) zero metabolic clearance within the tumour tissue. A perfused TME model was therefore developed in Chapter 3. Both single-capillary and vascular network models were used to evaluate the temporal and spatial heterogeneity of bubble-released oxygen deposition within the TME. Changes in oxygen diffusivity were found to have minimal effect on the predicted level of oxygen deposition, suggesting that reoxygenation of the nanobubbles is a more important mechanism for oxygen delivery to the tumour microenvironment. For approximately two minutes following intravenous injection, the

predicted oxygen deposition from the nanobubbles was also found to match the range of *in vivo* experimental data reported in Owen et al. (2016).

In conclusion, the results from this study (i) support the hypothesis of nanobubble reoxygenation and (ii) highlight the importance of vascular heterogeneity in determining the capability of oxygen carriers to alleviate tissue hypoxia in cancer therapy.

Future work should endeavour to further develop the models documented in this study, to include: nanobubble-specific dissolution physics, heterogeneity in the size distribution (and corresponding half-life) of the nanobubble population, interactions between multiple nanobubbles in suspension, and spatially varying vascular oxygenation in the systemic circulation. Incorporation of these mechanisms will hopefully reduce the disparity in timescales between the oxygenation predicted *in silico* and observed *in vivo*.

Investigating the pharmacokinetic and pharmacodynamic behaviour of both oxygen and an injected drug within the TME should form the next area of focus for this research. In order to maximise the adjuvant effect of the oxygenation, optimisation of the nanobubble properties and dosing regimen will required. Following these studies, *in vivo* investigations should be conducted to (i) support the results predicted *in silico* and (ii) investigate the efficacy of oxygen-enhanced cancer therapy in hypoxic tumour xenografts. If a substantial response is observed, continued work in the field could hopefully be translated into a viable treatment regimen for hypoxic cancers in the clinic and improved patient outcomes thereafter.

5 References

Adair, G. (1926). "The oxygen dissociation curve of hemoglobin." J Biol Chem 63: 529-545.

Alayash, A. I. (2014). "Blood substitutes: why haven't we been more successful?" Trends in Biotechnology 32(4): 177-185.

Arvanitis, C. D., et al. (2018). "Mechanisms of enhanced drug delivery in brain metastases with focused ultrasound-induced blood–tumor barrier disruption." Proceedings of the National Academy of Sciences 115(37): E8717-E8726.

Arvanitis, C. D., et al. (2019). "The blood–brain barrier and blood–tumour barrier in brain tumours and metastases." Nature Reviews Cancer: 1-16.

Aslan, S., et al. (2018). "Efficacy of perfusion CT in differentiating of pancreatic ductal adenocarcinoma from mass-forming chronic pancreatitis and characterization of isoattenuating pancreatic lesions." Abdominal Radiology.

Awwad, H. K., et al. (1986). "Intercapillary distance measurement as an indicator of hypoxia in carcinoma of the cervix uteri." International Journal of Radiation Oncology*Biology*Physics 12(8): 1329-1333.

Baish, J. W., et al. (1996). "Role of Tumor Vascular Architecture in Nutrient and Drug Delivery: An Invasion Percolation-Based Network Model." Microvascular Research 51(3): 327-346.

Baxley, P. T. and J. D. Hellums (1983). "A simple model for simulation of oxygen transport in the microcirculation." Annals of Biomedical Engineering 11(5): 401-416.

Beck, N. (2008). Diagnostic hematology, Springer Science & Business Media.

Bluemke, E. (2019). "Magnetic Resonance Imaging of Oxygen Nanocarriers." Transfer of Status Report, University of Oxford.

Borden, M. A. and M. L. Longo (2004). "Oxygen permeability of fully condensed lipid monolayers." Journal of Physical Chemistry B 108(19): 6009-6016.

Breward, C. J. W., et al. (2003). "A multiphase model describing vascular tumour growth." Bulletin of Mathematical Biology 65(4): 609-640.

Bush, A. J., et al. (2018). "Carboplatin Pharmacokinetic and Pharmacodynamic Mathematical Model for FUS-BBB Disruption in the Brain Tumour Microenvironment". Laidlaw Undergraduate Research Symposium. Sheldonian Theatre, University of Oxford

Byun, D. J., et al. (2017). "Cancer immunotherapy - immune checkpoint blockade and associated endocrinopathies." Nat Rev Endocrinol 13(4): 195-207.

Chang, J. H., et al. (2016). "Role of immune cells in pancreatic cancer from bench to clinical application: An updated review." Medicine (Baltimore) 95(49): e5541.

Chaplin DJ, H. M., Trotter MJ, Siemann DW (1998). "Therapeutic significance of microenvironmental factors." Blood Perfusion and Microenvironment of Human Tumors: Implications for Clinical Radiooncology: 133-143.
Chouaib, S., et al. (2017). "Hypoxic stress: obstacles and opportunities for innovative immunotherapy of cancer." Oncogene 36(4): 439-445.

Ciani, I., et al. (2004). "Effect of Surface Pressure on Oxygen Transfer across Molecular Monolayers at the Air/Water Interface: Scanning Electrochemical Microscopy Investigations Using a Mercury Hemispherical Microelectrode Probe." The Journal of Physical Chemistry B 108(12): 3801-3809.

Clark, A., Jr., et al. (1985). "Oxygen delivery from red cells." Biophys J 47(2 Pt 1): 171-181.

Daruwalla, J. and C. Christophi (2006). "Hyperbaric Oxygen Therapy for Malignancy: A Review." 30(12): 2112-2131.

Daşu, A., et al. (2003). "Theoretical simulation of tumour oxygenation and results from acute and chronic hypoxia." Physics in Medicine & Biology 48(17): 2829.

David R. Lide, e. (2005). "CRC Handbook of Chemistry and Physics." CRC Press.

De La Cruz, M. S. D., et al. (2014). "Diagnosis and management of pancreatic cancer." American family physician 89(8): 626-632.

De Pater, L. and J. Van den Berg (1964). "An electrical analogue of the entire human circulatory system." Medical electronics and biological engineering 2(2): 161-166.

Delaney, L. J., et al. (2019). "Breast Cancer Brain Metastasis Response to Radiation After Microbubble Oxygen Delivery in a Murine Model." Journal of Ultrasound in Medicine 38(12): 3221-3228.

Eggleton, C. D., et al. (2000). "Calculations of intracapillary oxygen tension distributions in muscle." 167(2): 123-143.

Faithfull, N. S. (1992). "Oxygen delivery from fluorocarbon emulsions--aspects of convective and diffusive transport." Biomater Artif Cells Immobilization Biotechnol 20(2-4): 797-804.

Ferrara, K., et al. (2007). "Ultrasound microbubble contrast agents: fundamentals and application to gene and drug delivery." Annu Rev Biomed Eng 9: 415-447.

Fick, A. (1855). "V. On liquid diffusion." The London, Edinburgh, and Dublin Philosophical Magazine and Journal of Science 10(63): 30-39.

Fix, S. M., et al. (2018). "Oxygen microbubbles improve radiotherapy tumor control in a rat fibrosarcoma model – A preliminary study." PLoS One 13(4): e0195667.

Garrido-Laguna, I. and M. Hidalgo (2015). "Pancreatic cancer: from state-of-the-art treatments to promising novel therapies." Nat Rev Clin Oncol 12(6): 319-334.

Gogna, R., et al. (2012). "Re-oxygenation causes hypoxic tumor regression through restoration of p53 wild-type conformation and post-translational modifications." 3(3): e286.

Goldman, D. (2008). "Theoretical models of microvascular oxygen transport to tissue." Microcirculation 15(8): 795-811.

Graeber, T. G., et al. (1996). "Hypoxia-mediated selection of cells with diminished apoptotic potential in solid tumours." Nature 379(6560): 88-91.

Graham, K. and E. Unger (2018). "Overcoming tumor hypoxia as a barrier to radiotherapy, chemotherapy and immunotherapy in cancer treatment." Int J Nanomedicine 13: 6049-6058.

Gramiak, R. and P. M. Shah (1968). "Echocardiography of the aortic root." Investigative radiology 3(5): 356-366.

Grimes, D. R., et al. (2014). "Oxygen consumption dynamics in steady-state tumour models." Royal Society Open Science 1(1): 140080.

Guyton, A. and J. E. Hall (2016). Guyton and Hall Textbook of Medical Physiology, Jordanian Edition E-Book, Elsevier.

Hasan, A. and M. Mazzone (2015). "Sixty shades of oxygen-an attractive opportunity for cancer immunotherapy." Ann Transl Med 3(13): 187.

Hatfield, S. M., et al. (2015). "Immunological mechanisms of the antitumor effects of supplemental oxygenation." Science Translational Medicine 7(277): 277ra230-277ra230.

Hernot, S. and A. L. Klibanov (2008). "Microbubbles in ultrasound-triggered drug and gene delivery." Advanced drug delivery reviews 60(10): 1153-1166.

Hill, A. V. (1910). "The possible effects of the aggregation of the molecules of haemoglobin on its dissociation curves." j. physiol. 40: 4-7.

Ho, Y.-J., et al. (2019). "Normalization of Tumor Vasculature by Oxygen Microbubbles with Ultrasound." Theranostics 9(24): 7370-7383.

Ho, Y.-J., et al. (2020). "Ultrasound in tumor immunotherapy: Current status and future developments." Journal of Controlled Release 323: 12-23.

Hockel, M. and P. Vaupel (2001). "Tumor hypoxia: definitions and current clinical, biologic, and molecular aspects." J Natl Cancer Inst 93(4): 266-276.

Horitsugi, G., et al. (2017). "Oxygen-15 labeled CO2, O2, and CO PET in small animals: evaluation using a 3D-mode microPET scanner and impact of reconstruction algorithms." EJNMMI Res 7(1): 91.

Jackson, C., et al. (2011). "Challenges in immunotherapy presented by the glioblastoma multiforme microenvironment." Clin Dev Immunol 2011: 732413.

Kabalnov, A., et al. (1998). "Dissolution of multicomponent microbubbles in the bloodstream: 1. theory." Ultrasound in Medicine & Biology 24(5): 739-749.

Khan, M. S., et al. (2018). "Oxygen-Carrying Micro/Nanobubbles: Composition, Synthesis Techniques and Potential Prospects in Photo-Triggered Theranostics." Molecules 23(9).

Khan, M. S., et al. (2018). "Engineering oxygen nanobubbles for the effective reversal of hypoxia." Artificial Cells, Nanomedicine, and Biotechnology 46(sup3): S318-S327.

Kheir, J. N., et al. (2013). "Bulk Manufacture of Concentrated Oxygen Gas-Filled Microparticles for Intravenous Oxygen Delivery." Advanced Healthcare Materials 2(8): 1131-1141.

Kleeff, J., et al. (2016). "Pancreatic cancer." Nat Rev Dis Primers 2: 16022.

Komar, G., et al. (2009). "Decreased blood flow with increased metabolic activity: a novel sign of pancreatic tumor aggressiveness." Clin Cancer Res 15(17): 5511-5517.

Koong, A. C., et al. (2000). "Pancreatic tumors show high levels of hypoxia." International Journal of Radiation Oncology*Biology*Physics 48(4): 919-922.

Kreissl, M. C., et al. (2006). "Noninvasive measurement of cardiovascular function in mice with high-temporal-resolution small-animal PET." Journal of Nuclear Medicine 47(6): 974-980.

Krogh, A. (1919). "The number and distribution of capillaries in muscles with calculations of the oxygen pressure head necessary for supplying the tissue." The Journal of Physiology 52(6): 409-415.

Krzywinska, E. and C. Stockmann (2018). "Hypoxia, Metabolism and Immune Cell Function." Biomedicines 6(2).

Kunk, P. R., et al. (2016). "From bench to bedside a comprehensive review of pancreatic cancer immunotherapy." J Immunother Cancer 4: 14.

Kwan, J. J. and M. A. Borden (2012). "Lipid monolayer dilatational mechanics during microbubble gas exchange." Soft Matter 8(17).

Kwan, J. J., et al. (2012). "Theranostic oxygen delivery using ultrasound and microbubbles." Theranostics 2(12): 1174-1184.

Labiano, S., et al. (2015). "Immune response regulation in the tumor microenvironment by hypoxia." Semin Oncol 42(3): 378-386.

Lee, C. T., et al. (2010). "Hypoxia-driven immunosuppression: a new reason to use thermal therapy in the treatment of cancer?" Int J Hyperthermia 26(3): 232-246.

Lequeux, A., et al. (2019). "Impact of hypoxic tumor microenvironment and tumor cell plasticity on the expression of immune checkpoints." Cancer Letters 458: 13-20.

Levenbrown, Y. and A. T. Costarino (2019). Chapter 17 - Edema. Nephrology and Fluid/electrolyte Physiology (Third Edition). W. Oh and M. Baum. Philadelphia, Elsevier: 271-290.

Li, M., et al. (2014). "Simulation study of pO2distribution in induced tumour masses and normal tissues within a microcirculation environment." Computer Methods in Biomechanics and Biomedical Engineering 17(4): 334-343.

Liang, F. and H. Liu (2005). "A closed-loop lumped parameter computational model for human cardiovascular system." JSME International Journal Series C Mechanical Systems, Machine Elements and Manufacturing 48(4): 484-493.

Lücker, A., et al. (2014). "A dynamic model of oxygen transport from capillaries to tissue with moving red blood cells." American Journal of Physiology-Heart and Circulatory Physiology 308(3): H206-H216.

Maxwell, P. H., et al. (1997). "Hypoxia-inducible factor-1 modulates gene expression in solid tumors and influences both angiogenesis and tumor growth." Proceedings of the National Academy of Sciences 94(15): 8104-8109.

McEwan, C., et al. (2015). "Oxygen carrying microbubbles for enhanced sonodynamic therapy of hypoxic tumours." J Control Release 203: 51-56.

McGuire, B. J. and T. W. Secomb (2001). "A theoretical model for oxygen transport in skeletal muscle under conditions of high oxygen demand." Journal of Applied Physiology 91(5): 2255-2265.

Michaels, A. D., et al. (2017). "CD47 Blockade as an Adjuvant Immunotherapy for Resectable Pancreatic Cancer." Clinical Cancer Research: clincanres.2283.

Moen, I. and L. E. B. Stuhr (2012). "Hyperbaric oxygen therapy and cancer--a review." Targeted oncology 7(4): 233-242.

Moradi, S., et al. (2016). "Artificial Blood Substitutes: First Steps on the Long Route to Clinical Utility." Clin Med Insights Blood Disord 9: 33-41.

Mossa, H. A. L. (2008). "Engineering Modeling of Human Cardiovascular System." Al-Nahrain Journal for Engineering Sciences 11(2): 307-314.

National Centre for Replacement, R. a. R. o. A. i. R. N. R. (2020). "Mouse - Decision Tree - Blood Sampling." Retrieved 15th November 2019, from https://www.nc3rs.org.uk/mouse-decision-tree-blood-sampling#:~:text=How%20much%20blood%20does%20a,x%200.025%20kg%20%3D%201.46%20ml.

Noman, M. Z., et al. (2014). "PD-L1 is a novel direct target of HIF-1α, and its blockade under hypoxia enhanced MDSC-mediated T cell activation." Journal of Experimental Medicine 211(5): 781-790.

Noman, M. Z., et al. (2019). "Improving Cancer Immunotherapy by Targeting the Hypoxic Tumor Microenvironment: New Opportunities and Challenges." Cells 8(9).

Owen, J., et al. (2016). "Reducing Tumour Hypoxia via Oral Administration of Oxygen Nanobubbles." PLoS One 11(12): e0168088.
Parpaleix, A., et al. (2013). "Imaging local neuronal activity by monitoring PO2 transients in capillaries." Nature Medicine 19(2): 241-246.

Patel S., M. A. (1998). "Modeling of Oxygen Transport in Blood-Perfluorocarbon Emulsion Mixtures." ASAIO Journal

Pidgeon, G. P., et al. (2001). "Vascular endothelial growth factor (VEGF) upregulates BCL-2 and inhibits apoptosis in human and murine mammary adenocarcinoma cells." British journal of cancer 85(2): 273-278.

Popel, A. S. (1989). "Theory of oxygen transport to tissue." Critical reviews in biomedical engineering 17(3): 257.

Rawla, P., et al. (2019). "Epidemiology of Pancreatic Cancer: Global Trends, Etiology and Risk Factors." World Journal of Oncology 10(1): 10-27.

Ryan, D. P., et al. (2014). "Pancreatic Adenocarcinoma." New England Journal of Medicine 371(11): 1039-1049.

Sander, R. (2015). "Compilation of Henry's law constants (version 4.0) for water as solvent." Atmospheric Chemistry and Physics 15(8): 4399-4981.

Sarkar, K., et al. (2009). "Growth and dissolution of an encapsulated contrast microbubble: effects of encapsulation permeability." Ultrasound Med Biol 35(8): 1385-1396.

Sciumè, G., et al. (2014). "Three phase flow dynamics in tumor growth." Computational Mechanics 53(3): 465-484.

Secomb, T. W. (2015). "Krogh-cylinder and infinite-domain models for washout of an inert diffusible solute from tissue." Microcirculation 22(1): 91-98.

Secomb, T. W., et al. (2004). "Green's function methods for analysis of oxygen delivery to tissue by microvascular networks." Ann Biomed Eng 32(11): 1519-1529.

Seekell, R. P., et al. (2016). "Oxygen delivery using engineered microparticles." Proceedings of the National Academy of Sciences 113(44): 12380-12385.

Shannon, A. M., et al. (2003). "Tumour hypoxia, chemotherapeutic resistance and hypoxia-related therapies." Cancer Treatment Reviews 29(4): 297-307.

Shpak, O., et al. (2016). Droplets, Bubbles and Ultrasound Interactions, Springer International Publishing: 157-174.

Shweiki, D., et al. (1995). "Induction of vascular endothelial growth factor expression by hypoxia and by glucose deficiency in multicell spheroids: implications for tumor angiogenesis." Proceedings of the National Academy of Sciences 92(3): 768-772.

Siegel, R. L., et al. (2018). "Cancer statistics, 2018." CA: A Cancer Journal for Clinicians 68(1): 7-30.

Stride, E. (2009). "Physical principles of microbubbles for ultrasound imaging and therapy." Cerebrovasc Dis 27 Suppl 2: 1-13.

Tao, L. N. (1978). "Dynamics of growth or dissolution of a gas bubble." The Journal of Chemical Physics 69(9): 4189-4194.

Tee, L. S., et al. (1966). "Molecular Parameters for Normal Fluids. Lennard-Jones 12-6 Potential." Industrial & Engineering Chemistry Fundamentals 5(3): 356-363.

Thompson, E. (2017). "Magnetic resonance imaging of oxygen carriers in treatment of hypoxic tumours." MRI Thesis.

Toma-Dasu, I. and A. Dasu (2013). "Modelling Tumour Oxygenation, Reoxygenation and Implications on Treatment Outcome." Computational and Mathematical Methods in Medicine 2013: 141087.

Tsoukias, N. M., et al. (2007). "A computational model of oxygen delivery by hemoglobin-based oxygen carriers in three-dimensional microvascular networks." Journal of theoretical biology 248(4): 657-674.

Unekawa, M., et al. (2010). "RBC velocities in single capillaries of mouse and rat brains are the same, despite 10-fold difference in body size." Brain research 1320: 69-73.

Vasilyeva, A. (2019). "Development of Ultrasound-Responsive Drug Delivery Agents for Combined Pharmacological Sonodynamics and Metabolic Therapy." Transfer of Status Report, University of Oxford.

Vaupel, P. and A. Mayer (2007). "Hypoxia in cancer: significance and impact on clinical outcome." Cancer and Metastasis Reviews 26(2): 225-239.

Webb, I. R., et al. (2010). "Dynamics of gas bubbles in time-variant temperature fields." Journal of Fluid Mechanics 663: 209-232.

Weinberg, R. A. (2013). "The Biology of Cancer, 2nd Edition." Garland Science.

Welter, M., et al. (2016). "Computational Model for Tumor Oxygenation Applied to Clinical Data on Breast Tumor Hemoglobin Concentrations Suggests Vascular Dilatation and Compression." PLoS One 11(8): e0161267.

Whiteside, T. L., et al. (2016). "Emerging Opportunities and Challenges in Cancer Immunotherapy." Clin Cancer Res 22(8): 1845-1855.

Wigerup, C., et al. (2016). "Therapeutic targeting of hypoxia and hypoxia-inducible factors in cancer." Pharmacol Ther 164: 152-169.

Wilson, W. R. and M. P. Hay (2011). "Targeting hypoxia in cancer therapy." Nat Rev Cancer 11(6): 393-410.
Wu, H., et al. (2013). "Acoustic characterization and pharmacokinetic analyses of new nanobubble ultrasound contrast agents." Ultrasound Med Biol 39(11): 2137-2146.

Zenewicz, L. A. (2017). "Oxygen Levels and Immunological Studies." Front Immunol 8: 324.

6 Appendices

6.1 Appendix 1: Table of Transport Model Parameters

Symbol	Value	Unit	Definition	Source
P_A	15	mmHg	Arterial Gauge Hydrostatic Pressure	Levenbrown and Costarino (2019)
P_V	0	mmHg	Venous Gauge Hydrostatic Pressure	Levenbrown and Costarino (2019)
L_p	1.395×10^{-10}	$m^3 \cdot s/kg$	Capillary Wall Hydraulic Conductivity	Guo and Fu (2012)
K	1.275×10^{-13}	$m^3 \cdot s/kg$	Interstitial Hydraulic Conductivity	Guo and Fu (2012)
ε_{int}	0.633	-	Interstitial Porosity	Arvanitis et al. (2018)
k_{int}	5.1×10^{-16}	m^2	Interstitial Permeability	Arvanitis et al. (2018)
μ	0.004	$Pa \cdot s$	Dynamic Viscosity	Arvanitis et al. (2018)
c_{Hb}	20.98	mol/m^3	Oyxgen Binding Capacity of Haemoglobin	Li et al. (2014)
D_{Hb}	1.44×10^{-11}	m^2/s	RBC Haemoglobin Solubility	Eggleton et al. (2000)
D_{RBC}	9.50×10^{-10}	m^2/s	RBC Oxygen Solubility	Eggleton et al. (2000)
D_{PL}	2.18×10^{-9}	m^2/s	Plasma Oxygen Solubility	Eggleton et al. (2000)
D_{int}	2.41×10^{-9}	m^2/s	Interstitial Oxygen Solubility	Eggleton et al. (2000)
α_{RBC}	9.98×10^{-6}	$s^2 \cdot mol/(kg \cdot m^2)$	RBC Oxygen Solubility	Eggleton et al. (2000)
α_{PL}	8.33×10^{-6}	$s^2 \cdot mol/(kg \cdot m^2)$	Plasma Oxygen Solubility	Eggleton et al. (2000)
α_{int}	1.15×10^{-5}	$s^2 \cdot mol/(kg \cdot m^2)$	Interstitial Oxygen Solubility	Eggleton et al. (2000)
M_{0T}	0.0122	$mol/(m^3 \cdot s)$	Maximal Oxygen Consumption Rate in Tumour Tissue	Baxley and Hellums (1983)
M_{0N}	0.00197	$mol/(m^3 \cdot s)$	Maximal Oxygen Consumption Rate in Healthy Tissue	Baxley and Hellums (1983)
n	2.7	-	Hill Equation Exponent	McGuire and Secomb (2001)

P_{S50}	34	mmHg	Oxygen Partial Pressure at 50% of Max. Haemoglobin Saturation	McGuire and Secomb (2001)
P_{M50}	0.35	mmHg	Oxygen Partial Pressure at 50% of Max. Metabolic Rate	McGuire and Secomb (2001)
L	600	µm	Single Capillary Length	Unekawa et al. (2010)
d	5	µm	Single Capillary Diameter	Parpaleix et al. (2013)
W	500	µm	Total Width of Single-Capillary Model Geometry (incl. Tissue)	Awwad et al. 1986
N_{Hb}	20.3	mol/m³	Total Haemoglobin Density	Eggleton et al. (2000)
N_{50}	0.0412	mol/m³	Oxygen Conc. Normalization Factor used in Lucker et al. (2014)	Clark et al. (1985)
φ	0.0212	mol/m³	RBC Source Term Coefficient for Free Oxygen	Calculated via Eq. 25
V_{molO2}	0.0254	m³/mol	Oxygen Molar Volume at 36.9 °C	Calculated via Ideal Gas Equation
κ_{Hb}	44	1/s	Haemoglobin Dissociation Rate Constant	Eggleton et al. (2000)
V_{TC}	1.17 x 10^{-8}	m³	Total Volume of Tumour Vasculature for 20g Mouse assuming 1% Tumour Blood Flow Fraction	NC3RS (2020) and Owen et al. (2016)
P_0	0	mmHg	Initial Condition for Interstitial Pressure	-
P_{O2RBC0}	90	mmHg	Initial Condition for Free Oxygen Partial Pressure (at Arterial End)	Lucker et al. (2014)
S_0	93.3	%	Initial Condition for Haemoglobin Saturation	Calculated via Eq. 21
c_0	19.6	mol/m³	Initial Condition for Free Oxygen Concentration (at Arterial End)	Calculated via Eq. 20

Table 4. Parameters and Initial Conditions used in the Oxygen Perfusion Model